Geophys. J. Int. (2004) **159,** 1032–1056 doi: 10.1111/j.1365-246X.2004.02442.x

Multiscale imaging of complex structures from multifold wide-aperture seismic data by frequency-domain full-waveform tomography: application to a thrust belt

C. Ravaut,[1] S. Operto,[1] L. Improta,[2] J. Virieux,[1] A. Herrero[2] and P. Dell'Aversana[3]

[1]*Géosciences Azur, CNRS UMR 6526, La Darse, Villefranche sur Mer, France. E-mail: operto@obs-vlfr.fr*
[2]*Istituto Nazionale di Geofisica e Vulcanologia, Via di Vigna Murata, Rome, Italy*
[3]*Eni S.p.a, Via Emilia 1, Milano, Italy*

Accepted 2004 August 2. Received 2004 May 28; in original form 2003 August 8

SUMMARY

An application of full-waveform tomography to dense onshore wide-aperture seismic data recorded in a complex geological setting (thrust belt) is presented.

The waveform modelling and tomography are implemented in the frequency domain. The modelling part is solved with a finite-difference method applied to the visco-acoustic wave equation. The inversion is based on a local gradient method. Only the *P*-wave velocity is involved in the inversion. The inversion is applied iteratively to discrete frequency components by proceeding from low to high frequencies. This defines a multiscale imaging in the sense that high wavenumbers are progressively incorporated in images. The linearized waveform tomography requires an accurate starting velocity model that has been developed by first-arrival traveltime tomography.

After specific pre-processing of the data, 16 frequency components ranging between 5.4 and 20 Hz were inverted. Ten iterations were computed per frequency component leading to 160 tomographic models. The waveform tomography has successfully imaged southwest-dipping structures previously identified from other geophysical data as being associated with high-resistivity bodies. The relevance of the tomographic images is locally demonstrated by comparison of a velocity–depth function extracted from the waveform tomography models with a coincident vertical seismic profiling (VSP) log available on the profile. Moreover, comparison between observed and synthetic seismograms computed in the (starting) traveltime and waveform tomography models demonstrates unambiguously that the waveform tomography successfully predicts for wide-angle reflections from southwest-dipping geological structures.

This study demonstrates that the combination of first-arrival traveltime and frequency-domain full-waveform tomographies applied to dense wide-aperture seismic data is a promising approach to quantitative imaging of complex geological structures. Indeed, wide-aperture acquisition geometries offer the opportunity to develop an accurate background velocity model for the subsequent waveform tomography. This is critical, because the building of the macromodel remains an open question when only near-vertical reflection data are considered.

Key words: finite-difference methods, thrust belt, traveltime and full waveform inversions, wide-aperture seismic data.

INTRODUCTION

Seismic imaging of complex structures characterized by strong lateral variations in the velocity field remains a challenge. Usually, the seismic imaging problem is applied to conventional surface–seismic multichannel reflection geometries which involve only near-vertical wave propagations (namely, short-angle reflections). In such geometries, the seismic imaging problem can be subdivided into two distinct tasks. Chronologically, the first one is the determination of a smooth background velocity model which describes the large-scale velocity distribution. This macromodel building is generally developed by traveltime tomography or migration-based velocity analysis. The second task makes use of this background velocity model to image the short-wavelength components of the structure by pre-stack depth migration/inversion, a well-established procedure for imaging complex structures (see Gray *et al.* 2001, for a review). By pre-stack depth migration/inversion, we define the class of quantitative pre-stack depth migration methods recast in the frame of seismic inverse theory (e.g. Lambaré *et al.* 1992; Thierry *et al.* 1999). Nevertheless, it is also well established that in the presence of complex media estimation of a reliable velocity macromodel for pre-stack depth migration/inversion is a very difficult task when only conventional multichannel seismic reflection data are available. Moreover, the precise definition of a reliable macromodel for pre-stack depth migration is still an open question which has been addressed only in a heuristic way (e.g. Operto *et al.* 2000). Indeed, conventional surface–seismic reflection geometries are not optimally designed for velocity estimation due to their limited aperture range. This precludes recordings of refracted and post-critical reflected waves at long offsets which are particularly sensitive to the large-scale velocity distribution.

Surface wide-aperture geometries, generally referred to as refraction geometries, are designed to yield sufficiently large source/receiver offsets in order to record waves refracted at the depths of investigation. Smooth macrovelocity models can then be developed either by refraction traveltime tomography (e.g. Toomey *et al.* 1994; Zelt & Barton 1998) or combined refraction/wide-angle reflection traveltime tomography (e.g. Zelt & Smith 1992; Korenaga *et al.* 2000; Improta *et al.* 2002; Hobro *et al.* 2003). In the latter case, one has to pick later-arriving wide-angle reflection phases consistently which is a non-trivial task, especially in the case of highly laterally heterogeneous media.

It is well known that velocity models of the Earth's interior developed by traveltime tomography are of limited spatial resolution. If wide-aperture experiments can be designed with closely spaced sources and receivers, such multifold acquisition geometries are amenable to 2-D full-waveform tomography (Pratt *et al.* 1996). By full-waveform tomography, we define the seismic inverse methods which account for the full-waveform of the seismograms recorded over a broad range of apertures spanning over the vertical incidence to the supercritical regime. Thanks to the wide-aperture geometry, full-waveform tomography theoretically allows for continuous mapping of wavelengths ranging from infinity (the average property of the medium) to half a wavelength (see Lambaré *et al.* 2003, for a resolution analysis which illustrates the relationship between aperture, temporal frequency and spatial resolution), hence, providing a tremendous improvement of spatial resolution compared with traveltime tomography (Pratt *et al.* 1996). Full-waveform tomography is generally based on a linearization of the inverse problem which requires the definition of a starting model. Indeed, traveltime tomography is the most well-adapted tool for developing such a starting model (e.g. Pratt & Goulty 1991).

Note that the seismic imaging problem was previously defined as two uncoupled tasks (macromodel building and small-wavelength imaging) when applied to seismic reflection data because there is generally a deficit of intermediate wavelengths between the spectrum of the large-scale background model and the small-wavelength migrated section (Jannane *et al.* 1989). In practice, this uncoupling requires the background macromodel to remain the same during a linear iterative pre-stack depth migration/inversion (Lambaré *et al.* 1992). This contrasts with combined traveltime and full-waveform tomography from wide-aperture seismic data which provides the framework to image a broad and continuous range of wavelengths in one single integrated imaging approach. Practically, this is illustrated by the fact that the successive application of traveltime and full-waveform tomography is performed in a non-linear iterative way, namely, the traveltime tomography model is updated by addition of the full-waveform tomography model perturbations to provide an improved model.

Full-waveform tomography developed rapidly in the late 1980s driven by the work of Tarantola and his colleagues (Tarantola 1987). Nevertheless, applications of full-waveform tomography to real data remained rare until recently because of the computational cost of the method, the difficulty of designing seismic experiments which combine multiple-fold and large-aperture coverage and the extreme sensitivity of full-waveform tomography to noise and errors in the starting model. With the rapid advent of large parallel computers and with the increase of new seismic acquisition technologies, the first two limitations have almost been removed today, at least for 2-D problems. The objective of this paper is to assess whether a waveform tomography strategy can be designed to overcome the third methodological difficulty.

Many successful wavefield tomography schemes are based on direct methods such as finite difference to model wave propagation since these forward modelling techniques allow us to take into account arbitrarily complex models and to model the full complexity of the wavefields (e.g. Virieux 1986).

2-D full-wavefield tomography based on finite-difference methods was originally developed in the time–space domain (e.g. Tarantola 1984; Gauthier *et al.* 1986; Crase *et al.* 1990, 1992; Pica *et al.* 1990; Sun & McMechan 1992). The full-wavefield tomography problem is solved by an iterative local, linearized approach using a gradient method (e.g. Tarantola 1987). At each iteration, the residual wavefield (namely, the difference between the observed data and the wavefield predicted by the starting model) is minimized in a least-squares sense. The process is iterated non-linearly, which means that the final model of the iteration n is used as a starting model for the subsequent iteration $n + 1$.

The main drawback of the time-domain approach is that it is computationally very expensive since the finite-difference forward modelling must be fully computed twice per shot (once for a source position corresponding to the shot and once for a source considering simultaneously residual excitations at all station positions).

A recent application of time-domain full-waveform tomography to wide-aperture marine streamer data was presented by Shipp & Singh (2002). However, the application of Shipp & Singh (2002) remained limited to the imaging of a quasi-tabular medium.

To circumvent limitations of the time-domain approach Pratt & Worthington (1990); Pratt *et al.* (1998) developed 2-D full-waveform modelling and tomography in the frequency domain. In the frequency domain, finite-difference modelling of wave propagation is very well adapted to multisource problems which characterize seismic acquisitions (Pratt & Worthington 1990; Stekl & Pratt 1998). Moreover, attenuation can be easily implemented in frequency-domain modelling algorithms using complex velocities.

The inverse problem is also solved in the frequency domain (Pratt *et al.* 1998). The Fourier transform provides a decomposition of the data into monochromatic wavefields that allows for the inversion of one or several discrete frequency data components at a time and manages a compact volume of data (one frequency component of a seismic trace is stored by a complex number). The inversion proceeds from low- to high-frequency components to inject progressively higher wavenumbers in the tomographic model. This multiscale approach applied to selected subdata sets sensitive to different scales of the medium helps to mitigate the non-linearity of the inverse problem (Pratt *et al.* 1996). Moreover, if the acquisition geometry contains wide-angle components, a strong redundancy in the wavenumber domain is present in the data (Pratt & Worthington 1990). This redundancy results from the combined influence of the source frequency and the source–receiver aperture on the resolution power of the seismic imaging processing (i.e. the wavenumber range which can be imaged by the data). One can partly decimate this redundancy by limiting the number of frequency components to be inverted. This is another key point which, in addition to the efficiency of the frequency-domain forward-modelling problem, makes frequency-domain waveform tomography significantly less computationally expensive than time-domain waveform tomography.

The full-waveform tomography was mainly applied to cross-hole data which are characterized by wide-aperture propagations (Pratt & Worthington 1990; Pratt & Goulty 1991; Pratt 1999; Pratt & Shipp 1999). An application to conventional multichannel seismic reflection data was also presented by Hicks & Pratt (2001) but was limited to shallow, sub-horizontal events due to the inherent limitations of the acquisition geometry mentioned above (Hicks & Pratt 2001). An application of combined traveltime tomography and frequency-domain full-waveform tomography to ultrasonic data was presented by Dessa & Pascal (2003). Dessa & Pascal (2003) have shown that traveltime tomography provides a sufficiently accurate starting model to initiate the subsequent waveform tomography even in the case of a very contrasted model (i.e. a velocity model involving velocity contrast between 1.5 km s^{-1} and 4.5 km s^{-1}). An assessment of the method when applied to surface wide-angle seismic data was presented by Pratt *et al.* (1996) in the framework of a crustal-scale synthetic experiment. However, assessment of the method when applied to real refraction data recorded in a complex geological environment is still required.

This paper is the first attempt to fill this gap. We present an application of frequency-domain full-waveform tomography to surface onshore seismic data collected with a multifold wide-angle aperture geometry in a very complex geological setting (i.e. a thrust belt). The starting model used to initiate the waveform tomography was developed by non-linear traveltime tomography. The results of the non-linear traveltime tomography have already been presented by Improta *et al.* (2002).

In the first part of the paper we briefly present an outline of the method that was used. Rather than rehashing the theory of frequency-domain waveform modelling/tomography that was extensively introduced by Pratt & Worthington (1990), Pratt *et al.* (1998, 1996) and Pratt (1999), we detail some numerical aspects of our implementation of the full-waveform modelling/tomography algorithms.

In the second part, we present a synthetic example to validate the full-waveform tomography algorithm when applied to complex media imaging. The dip section of the SEG/EAGE 3-D overthrust model is used for this test.

In the third part, we present the application of our approach to onshore wide-aperture data recorded in the Southern Apennine thrust belt (Italy). We detail the data pre-processing specifically designed for the waveform tomography. Since our full-waveform tomography involves only the *P*-wave velocity (monoparametric acoustic inversion), the main goal of our pre-processing is to transform the data such that wavefields after pre-processing reflect as well as possible the acoustic approximation.

The waveform tomography velocity models are shown at different stages of the multiscale tomography to illustrate how high wavenumbers are progressively incorporated in the models. The relevance of the waveform tomography models is verified by comparison with other geophysical studies of the target (vertical seismic profile, resistivity section), analysis of the data fit in the time and frequency domains and structural interpretation of the waveform tomography images.

METHODS

First-arrival traveltime inversion

The imaging procedure starts with non-linear first-arrival traveltime tomography (Herrero *et al.* 1999) used to determine a large-scale velocity macromodel. A brief outline of the method is given here and the reader is referred to Improta *et al.* (2002) for a detailed description of the method.

The inversion technique combines the multiscale approach of Lutter *et al.* (1990) and the use of a non-linear optimization scheme.

Only first-arrival traveltimes were considered to develop a starting model for full-waveform tomography although the traveltime tomography method can also handle reflection traveltimes to map interfaces (Improta *et al.* 2002). Inversion of first-arrival traveltimes gives a smooth background model. Subsequent mapping of discontinuities (i.e. the small wavenumbers) was left to the subsequent full-waveform tomography.

First-arrival traveltimes are computed by the finite-difference eikonal solver of Podvin & Lecomte (1991). The velocity values at the cells of the finite-difference mesh are interpolated from a coarse grid of 2-D bicubic spline nodes which constitute the model parameters for the no- linear traveltime tomography.

The inversion procedure consists of a succession of inversion runs performed by progressively refining the velocity grid. At each inversion run, the minimum value of the cost function ($\mathcal{L}2$ norm) is searched for by a non-linear optimization scheme that combines global (Monte Carlo) and local search (downhill simplex) algorithms. The multiscale procedure is halted based on two stopping criteria: the decrease of the root mean square (RMS) traveltime residual and the model resolution assessed by *a posteriori* checkerboard resolution tests (Improta *et al.* 2002). Note that the initiation of the tomography at the coarser level doesn't require a starting model: a velocity model on the coarsest grid is found by a global Monte Carlo search which can be achieved at low computational cost on this coarse grid.

Frequency-domain full-waveform tomography

The theory of frequency-domain waveform modelling and tomography has already been extensively presented by Jo *et al.* (1996), Stekl & Pratt (1998) and Hustedt *et al.* (2004) and by Pratt & Worthington (1990), Pratt *et al.* (1996, 1998), Pratt (1999), Pratt & Shipp (1999), Hicks & Pratt (2001) and Dessa & Pascal (2003) for the modelling and tomography parts respectively. Therefore, only a brief introduction to the method is given here.

Finite-difference waveform modelling

The 2-D visco-acoustic wave equation is written in the frequency domain as

$$\frac{\omega^2}{\kappa(x,z)} P(x,z,\omega) + \frac{\partial}{\partial x}\left(\frac{1}{\rho(x,z)}\frac{\partial P(x,z,\omega)}{\partial x}\right) + \frac{\partial}{\partial z}\left(\frac{1}{\rho(x,z)}\frac{\partial P(x,z,\omega)}{\partial z}\right) = S(x,z,\omega) \qquad (1)$$

where $\rho(x,\ z)$ is density, $\kappa(x,\ z)$ is the bulk modulus, ω is frequency, $P(x,z,\omega)$ is the pressure field and $S(x,z,\omega)$ is the source. Attenuation is easily implemented in this equation using complex velocities $\tilde{c}$ (Toksoz & Johnston 1981).

$$\frac{1}{\tilde{c}} = \frac{1}{c}\left(1 + \frac{i}{2Q}\operatorname{sign}(\omega)\right) \tag{2}$$

where Q is the quality factor and ω is the angular frequency. The complex valued bulk modulus is given by $\tilde{\kappa}(x, z) = \rho(x, z)\tilde{c}(x, z)^2$.

Because density and quality factor are considered constant in this study, the visco-acoustic wave equation reduces to the scalar wave equation

$$\frac{\omega^2}{\tilde{c}^2(x, z)} P(x, z, \omega) + \triangle P(x, z, \omega) = S(x, z, \omega) \tag{3}$$

where $\triangle$ denotes the Laplacian operator. The visco-acoustic and scalar wave equations (eqs 2 and 3) can be written in matrix form as

$$\mathbf{A}\mathbf{p} = \mathbf{s} \tag{4}$$

where the complex-valued impedance matrix $\mathbf{A}$ depends on the frequency and properties of the medium. The 2-D pressure $\mathbf{p}$ and source $\mathbf{s}$ fields at one frequency ω are stored as vectors of dimension $nx \times nz$ where nx and nz denote the dimensions of the regular finite-difference grid with a grid interval h. The pressure field is obtained by solving the system of linear equations. If this system is solved by a direct method (for example, LU factorization of the matrix $\mathbf{A}$ followed by forward and backward substitutions), the solutions for a large number of source terms can be obtained efficiently, once the matrix $\mathbf{A}$ has been factorized, as shown by the following system:

$$\mathbf{LU}\left[\mathbf{p}_1\mathbf{p}_2 \ldots \mathbf{p}_n\right] = \left[\mathbf{s}_1\mathbf{s}_2 \ldots \mathbf{s}_n\right]. \tag{5}$$

This makes frequency-domain methods very appealing for multisource simulations (e.g. Pratt & Worthington 1990). The wave equation (eq. 1) is discretized in a finite-difference sense using the so-called mixed-grid approach described in Jo *et al.* (1996); Stekl & Pratt (1998); Hustedt *et al.* (2004). The partial derivatives in eqs (1) and (3) are discretized using parsimonious staggered-grid second-order finite-difference schemes on two coordinate systems (the classic Cartesian system and a system rotated by 45°) (Hustedt *et al.* 2004). The derivative approximations in the two coordinate systems are combined linearly in order to minimize phase–velocity dispersion (Jo *et al.* 1996). The mass acceleration term $\omega^2/\kappa(x, z)$ is approximated using a weighted average over nine surrounding grid points similar to an antilump mass approach in finite-element modelling (Jo *et al.* 1996). The absorbing boundary conditions on the edges of the model consist of a combination of the 45° paraxial condition of Clayton & Engquist (1977) and the perfectly matched layer (PML) sponge-like condition (Berenger 1994). A description of our implementation of the PML condition for the wave equation is provided in Hustedt *et al.* (2004). The solution of the system (eqs 4 and 5) is computed through an optimized minimum-order scheme developed by Davis & Duff (1997).

Full-waveform tomography: theory and numerical aspects

The linearized waveform inversion is solved in the frequency domain by a classic gradient method (see for example Pratt *et al.* 1998, for a detailed derivation of the gradient direction). In its standard form, the gradient method provides the following relation between model perturbations and data residuals:

$$\delta\mathbf{m} = -\alpha\nabla_m E = -\alpha\operatorname{Re}\{\mathbf{J}^{\mathrm{T}}\delta\mathbf{d}^*\} \tag{6}$$

where $\delta\mathbf{m}$ is the model perturbation (the updated model $\mathbf{m}$ is related to the starting model $\mathbf{m}_0$ by $\mathbf{m} = \mathbf{m}_0 + \delta\mathbf{m}$), $\nabla_m E$ is the gradient of the cost function, α is a step length, $\mathbf{J}^{\mathrm{T}}$ is the transpose of the Jacobian matrix (namely, the Frechét derivative matrix), $\delta\mathbf{d}^*$ is the conjugate of the data residual and Re denotes the real part of a complex number.

The elements of the column of the Jacobian matrix corresponding to the ith parameter m_i are given by

$$\frac{\partial\mathbf{p}}{\partial m_i} = -\mathbf{A}^{-1}\frac{\partial\mathbf{A}}{\partial m_i}\mathbf{p} \tag{7}$$

where $\mathbf{p}$ denotes the forward-modelled pressure wavefields (Pratt *et al.* 1998, eqs 15 and 16). Inserting the expression for the partial derivative (eq. 7) in the inversion formula (eq. 6) and exploiting the source–receiver reciprocity principle, it can be shown that the ith model perturbation is given by (Pratt *et al.* 1998)

$$\delta m_i = \alpha\operatorname{Re}\left\{\mathbf{p}^{\mathrm{T}}\left[\frac{\partial\mathbf{A}^{\mathrm{T}}}{\partial m_i}\right]\mathbf{A}^{-1}\delta\mathbf{d}^*\right\}. \tag{8}$$

Eq. (8) indicates that the gradient is formed by a zero-lag convolution of the forward-modelled wavefield $\mathbf{p}$ with the backward-propagated residuals $\mathbf{A}^{-1}\delta\mathbf{d}^*$ (see Pratt *et al.* (1998) for a more extensive introduction of the gradient interpretation). The matrix $\partial\mathbf{A}^{\mathrm{T}}/\partial m_i$ is easily computed numerically from the finite-difference stencil discretizing matrix $\mathbf{A}$. This matrix is extremely sparse since it represents an operator of local support centred around the position of parameter i (Pratt *et al.* 1998). Eq. (8) requires the computation of only two forward-modelling problems (i.e. forward and backward substitutions) per shot position: the first forward problem computes wavefield $\mathbf{p}$ for a source located at the shot position. The second computes the backward-propagated residual wavefield $\mathbf{A}^{-1}\delta\mathbf{d}^*$ using a 'composite' source formed by the assemblage of the data residuals. One can see that the explicit computation of the Jacobian matrix is avoided in this formalism (Pratt *et al.* 1998).

In order to provide stable and reliable results, some scaling and regularizations must be applied to the gradient method. The inversion formula used in this study is given by

$$\begin{aligned}\delta\mathbf{m} &= -\alpha(\operatorname{diag}\mathbf{H}_a + \epsilon\mathbf{I})^{-1}\mathbf{C}_m\nabla_m E\\ &= -\alpha(\operatorname{diag}\mathbf{H}_a + \epsilon\mathbf{I})^{-1}\mathbf{C}_m\operatorname{Re}\{\mathbf{J}^{\mathrm{T}}\delta\mathbf{d}^*\}\end{aligned} \tag{9}$$

where $\operatorname{diag}\mathbf{H}_a = \operatorname{diag}\operatorname{Re}\{\mathbf{J}^{\mathrm{T}}\mathbf{J}^*\}$ denotes the diagonal elements of approximate Hessian $\mathbf{H}_a$.

The diagonal of the approximate Hessian provides a preconditioner of the gradient which properly scales the tomographic model (Shin *et al.* 2001). Illustrative synthetic examples of the efficiency of this scaling are presented in Shin *et al.* (2001). The damping parameter ϵ is used to avoid numerical instability (i.e. division by zero). Increasing the value of ϵ mitigates the effect of the scaling (this parameter has a comparable effect to pre-whitening in the frame of deconvolution processing).

Note that calculation of the diagonal elements of the approximate Hessian requires the explicit calculation of the Jacobian matrix $\mathbf{J}$. This can be achieved at reasonable cost by exploiting the source–receiver reciprocity principle (Shin *et al.* 2001). The explicit computation of the Jacobian matrix requires the computation of the Green's functions for sources located at each shot and receiver position (numerically, this corresponds to one forward and backward substitution per source and receiver position to solve the system of eqs 5) while it is recalled that the classic gradient algorithm (eq. 8) requires the computation of only two Green's functions per shot position. Considering a classic refraction experiment for which each receiver records all the shots, the number of forward problems to be solved without explicit computation of the Jacobian will be $2 \times N_s$

where N_s is the number of shots. The explicit computation of the Jacobian will require the computation of $N_s + N_r$ forward problems where N_r is the number of receivers. If the number of receivers is close to the number of shots (as may be the case in the case of oil exploration surveys conducted on land), one can note that the explicit computation of the Jacobian can be achieved at a minimal extra cost.

The matrix $\mathbf{C}_m$ is a smoothing regularization operator. It was implemented in the form of a 2-D Gaussian spatial filter whose correlation lengths are adapted to the inverted frequency component. Given an average velocity in the model c_0 and a frequency component υ, the horizontal and vertical correlation lengths of the Gaussian filter τ_x and τ_z, are defined as fractions perc_x and perc_z of the average wavelengths $\lambda = c_0/\upsilon$, namely, $\tau_x = \mathrm{perc}_x \times \lambda$ and $\tau_z = \mathrm{perc}_z \times \lambda$.

The perturbation model $\delta\mathbf{m}$ is discretized on a Cartesian grid with horizontal and vertical grid intervals denoted by h_x and h_z. This grid is a decimated version of the finite-difference grid used for the forward problem: $h_x = \mathrm{decim}_x \times h$ and $h_z = \mathrm{decim}_z \times h$ where it is reminded that h is the grid interval of the finite-difference grid used for forward modelling. Once a perturbation model has been computed on the inversion grid, it is linearly interpolated on the forward-modelling grid in order to proceed to the next iteration.

In summary, the inversion program requires a judicious estimation of the following parameters: the regularization parameter ϵ, the smoothing parameters perc_x and perc_z, the grid decimation parameters decim_x and decim_z, the number of iterations per frequency N_{it}, the number of frequencies to be inverted N_υ and the values of these frequencies $\upsilon(i)$, $i = 1, N_\upsilon$.

One iteration of the inversion algorithm is subdivided into four main parts: (1) computation of the Green's functions for each shot and receiver positions; (2) computation of the data residuals and RMS misfit; (3) computation of the Jacobian matrix and the preconditioned gradient; (4) computation of the step length α by a line-search technique, calculation of the perturbations and updated models. In our inversion program, only the velocity parameter is involved in the inversion although the forward modelling program can account for velocity, density and attenuation.

Source estimation

The application of full-waveform tomography requires the estimation of the temporal source function (eq. 4) (e.g. Pratt 1999). For onshore data, two main approaches are possible: a source wavelet can be estimated by predictive deconvolution of the data or it may be estimated by solving a linear inverse problem whose associated forward problem relates the data to the source function. This second approach was used in the synthetic and real data examples presented hereafter.

The forward problem associated with this linear inverse problem (Pratt 1999) is given by

$$\mathbf{A}\mathbf{p} = o\mathbf{s}, \tag{10}$$

where $\mathbf{s}$ is an *a priori* estimate of the source term and o is a complex-valued scalar to be determined at each frequency component that is inverted. The least-squares solution is given by Pratt (1999)

$$o = \frac{\mathbf{p}_0{}^{\mathrm{T}}\mathbf{d}^*}{\mathbf{p}_0{}^{\mathrm{T}}\mathbf{p}_0{}^*} = \frac{\sum_{i=1}^{N} p_{0i} d_i^*}{\sum_{i=1}^{N} p_{0i} p_{0i}^*} \tag{11}$$

where $\mathbf{d}$ are the data and $\mathbf{p}_0$ is the wavefield computed for the source estimate $\mathbf{s}$. In eq. (11), the scalar o is computed by summation over the full data set, N denoting the total number of source–receiver pairs. This approach requires an estimation of the velocity structure. A strong assumption associated with this approach is that the velocity structure used to estimate o accurately predicts the data if the source is known.

The source estimation was directly implemented in the waveform tomography algorithm before estimation of the data residuals rather than prior to the waveform inversion. The source term was estimated in the frequency domain for each frequency component to be inverted. Moreover, one frequency component of the source was re-estimated at each iteration of the frequency component inversion. The velocity model used for the source estimation was the starting velocity model used for the subsequent waveform inversion iteration. One drawback of this approach is that the source signature used in the inversion cannot be visualized in the time domain since it is estimated only at the frequency components to be inverted and the source term computed at one frequency is updated over iterations.

SYNTHETIC EXAMPLE: THE OVERTHRUST MODEL

We present here an application of full-waveform tomography to a synthetic wide-aperture seismic data set computed in a 2-D dip section of the 3-D onshore overthrust model.

The onshore 3-D overthrust model is composed of a complex thrusted sedimentary succession constructed on top of a structurally decoupled extensional and rift basement block (Fig. 1a) (Aminzadeh *et al.* 1995). The top of the model is characterized by an erosional truncation leading to important lateral velocity variations at the surface (weathering zone). The overthrust model contains small-scale features such as thin beds, lenses, pinchouts and channels. More details about the geology of the overthrust model can be found in Aminzadeh *et al.* (1995).

The dip section of the overthrust model used in this paper has dimensions of 20 × 3.5 km. The finite-difference grid used to discretize the overthrust model has a mesh spacing of 25 m in the horizontal and vertical directions.

Seismic imaging of the overthrust model from multichannel seismic reflection data by 2.5-D and 3-D ray-based pre-stack depth migration/inversion was presented in Operto *et al.* (2003). These imaging results obtained from seismic reflection data can be compared with those presented here to assess the benefit provided by wide-aperture acquisition geometry in terms of wavenumber resolution (i.e. a broader wavenumber bandwidth can be recovered from wide-aperture acquisition geometries by incorporating low wavenumbers in the spectrum).

2-D wide-aperture seismic data were computed in the dip section of the overthrust model with a wide-aperture acquisition geometry representative of the real data set processed in the following section. The acquisition geometry consists of a line of 200 shots with a spacing of 100 m and recorded by a coincident line of 200 receivers also with a 100 m spacing. Shots and receivers are at 25 m depth. The source is the second derivative of a Gaussian function with a dominant frequency of 10 Hz (Fig. 2a). An example of a common shot gather is shown in Fig. 2(a).

The starting model that was used to initiate waveform tomography was obtained by smoothing the true model with a 2-D Gaussian filter with a horizontal and vertical correlation lengths of 500 m (Fig. 1b). The wavelength content of this background model reasonably reflects that of the traveltime tomography model used as a

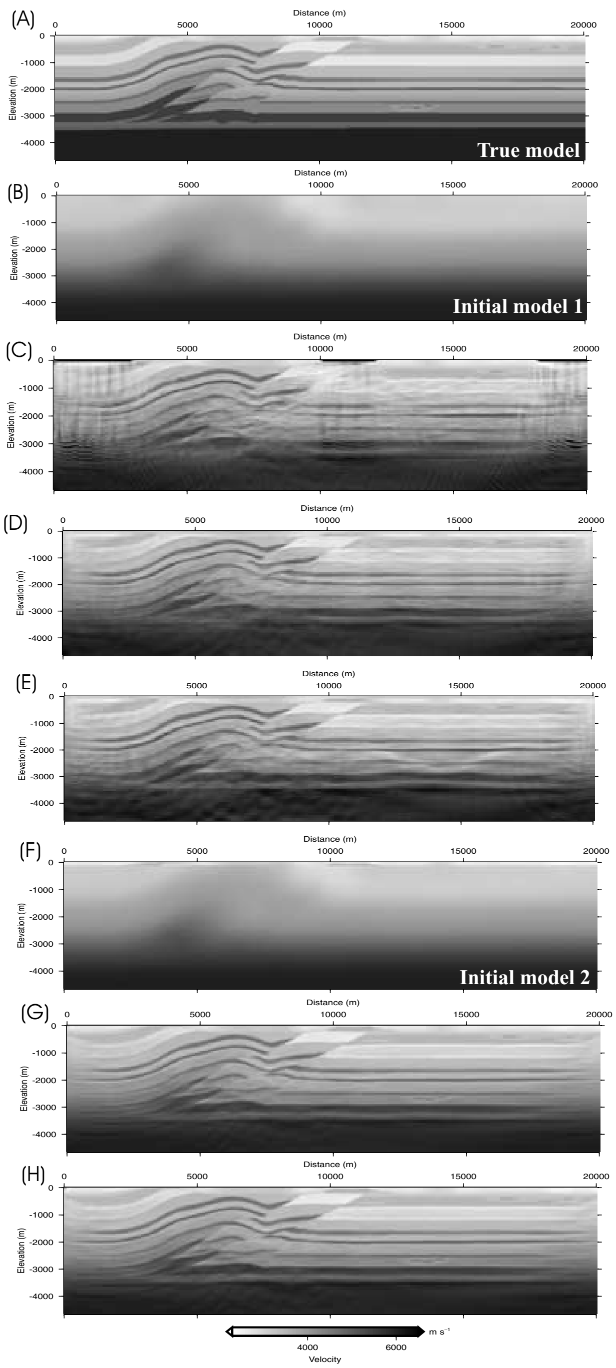

Figure 1. (a) Dip section of the overthrust model. (b) Dip section of the overthrust model smoothed with a 2-D Gaussian filter using horizontal and vertical correlation lengths of 500 m. This model was used as a starting model for waveform tomography to obtain the final models of parts (c)–(e). (c) Final waveform tomography model obtained from the starting model shown in (b). Note some instabilities in the subsurface velocity estimation (for example, between 10 and 12 km distance) which lead to noisy tomographic images. (d) Same as (c) except that the first 100 m of the waveform tomography model was left unperturbed during the waveform tomography. Note the noise reduction compared with (c). (e) Same as (d) except that the source was unknown and estimated in the waveform tomography program. (f) Same as (b) except that the true velocity model is incorporated between 0 and 100 m depth. This model was used as a starting model for waveform tomography to obtain the final models in (g) and (h). (g) Waveform tomography model obtained from the starting model of (f). (h) Same as (g) except that the source was unknown and estimated in the waveform tomography program.

starting model for the full-waveform tomography of the real data set. Synthetic data computed in this starting model are shown in Fig. 2(b) together with residuals (i.e. difference between seismograms of Figs 2a and b).

Thirteen frequencies between 6 and 20.6 Hz were sequentially inverted. Ten iterations per frequency were used. The damping parameter ϵ was set to 0.005.

The final model is shown in Fig. 1(c). Although the main features of the overthrust model (thrusts, sedimentary layering) can be identified in the figure, one can note that the waveform tomography image is polluted by several noises. These noises result from strongly overestimated velocities near the subsurface in the weathering zone of the overthrust model (see, for example, between 10 and 12 km distance). These artificial bright spots of high velocities lead to strong amplitude diffractions in the computed wavefield (and hence high-amplitude residuals) which are wrongly backpropagated into the medium.

To avoid these near-surface instabilities, the velocities between 0 and 100 m depth were fixed during waveform tomography. The final waveform tomography model is shown in Fig. 1(d). Most of the artefacts of the model of Fig. 1(c) have been significantly mitigated. The model of Fig. 1(e) was obtained using the same approach as that for the model of Fig. 1(d) except that the source excitation was unknown and estimated in the waveform tomography program using the approach described in the section entitled Source estimation. Synthetic seismograms computed in the waveform tomography models of Figs 1(d) and (e) are shown in Figs 2(c) and (e) respectively. One can note that the reflections have been reasonably well explained but that high-amplitude refracted waves remained in the residuals. Again, these high-amplitude residuals are wrongly backpropagated into the medium leading to noise in the waveform tomography image. However, the amplitude of this noise is reasonably small when the acquisition is highly redundant as in the case of this synthetic test. Thanks to this redundancy (the huge number of constructive summations dominate the limited number of erroneous ones), a reasonably good image of the deeper structure can be obtained even when the subsurface velocities are not accurate (Figs 1d and e). The high-amplitude refracted waves propagate in the subsurface structure where the velocities have been fixed. This can be checked in Figs 2(d) and (f) which show synthetic seismograms computed in the waveform tomography models of Figs 1(d) and (e) except that velocities of the smooth starting model were replaced by velocities of the overthrust dip section between 0 and 100 m depth. The high-amplitude waves refracted in the subsurface are no longer observed in the residuals.

The cost function plotted with respect to frequency components corresponding to the two applications of Figs 1(d) and (e) is shown in Figs 3(a) and (b). The cost function is poorly reduced, although the velocity structure has been reasonably well imaged. This poor cost-function reduction results from the fact that residuals are dominated by the high-amplitude refracted waves in the smoothed subsurface layer (Figs 2c and e). Since this surface layer is kept fixed, waveform tomography does not have the freedom to reduce the high-amplitude residual part resulting from the inaccuracies in the subsurface.

Results of this latter test show that a careful analysis of waveform tomography results must be carried out before drawing conclusions on the relevance of waveform tomography models since localized errors in the model may lead to a poor cost reduction, although a good imaging of the deeper structure was obtained. Such analysis must incorporate qualitative and quantitative interpretation of synthetic seismograms and data residuals, comparison with other complementary geophysical studies of the target and geological expertise.

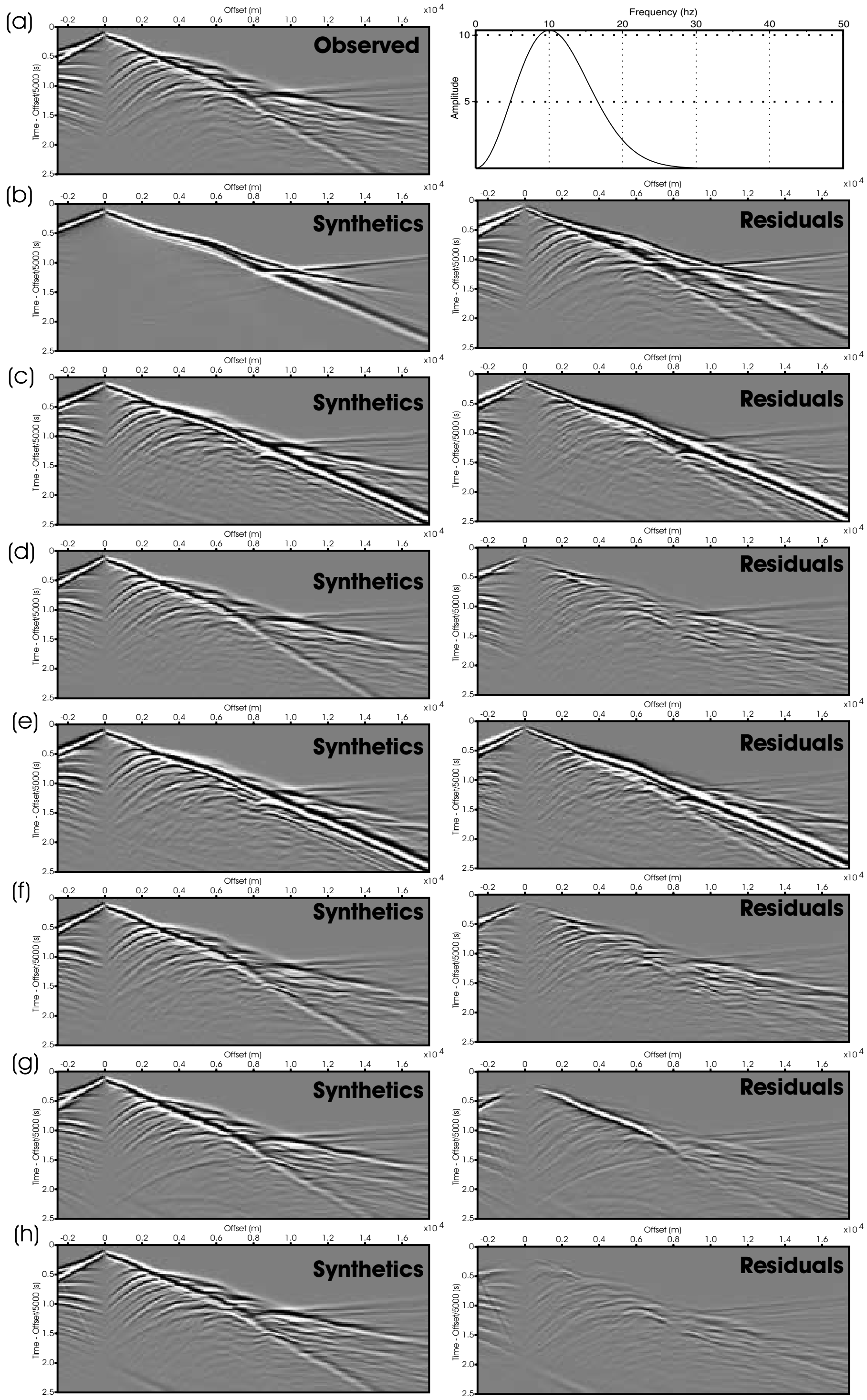

Figure 2. (a) Seismograms computed in the overthrust model (Fig. 1a) for a shot located at a distance of 2.5 km. A gain with offset is applied to the amplitudes. The right-hand parts shows the spectral amplitude of the source. (b) Left: seismograms computed in the smooth initial model of Fig. 1(b). Right: residuals (i.e. the difference between the seismograms in the left panels of parts (a) and (b)). All the seismograms are plotted on the same scale as that in part (a). (c) Left: seismograms computed in the waveform tomography model of Fig. 1(d). Right: residuals between these seismograms and those of Fig. 1(a). (d) Left: seismograms computed in a modification of the waveform tomography model of Fig. 1(d). Velocities between 0 and 100 m depth of the waveform tomography model of Fig. 1(d) were replaced by those of the true model (Fig. 1a). The rest of the waveform tomography model of Fig. 1(d) was left unchanged. Right: residuals between these seismograms and those of Fig. 1(a). (e) Left: seismograms computed in the waveform tomography model of Fig. 1(e). Right: residuals between these seismograms and those of Fig. 1(a). (f) Left: seismograms computed in a modification of the waveform tomography model of Fig. 1(e). Velocities between 0 and 100 m depth of the waveform tomography model of Fig. 1(e) were replaced by those of the true model (Fig. 1a). The rest of the waveform tomography model of Fig. 1(e) was left unchanged. Right: residuals between these seismograms and those of Fig. 1(a). (g) Left: seismograms computed in the waveform tomography model of Fig. 1(g). Right: residuals between these seismograms and those of Fig. 1(a). (h) Left: seismograms computed in the waveform tomography model of Fig. 1(h). Right: residuals between these seismograms and those of Fig. 1(a).

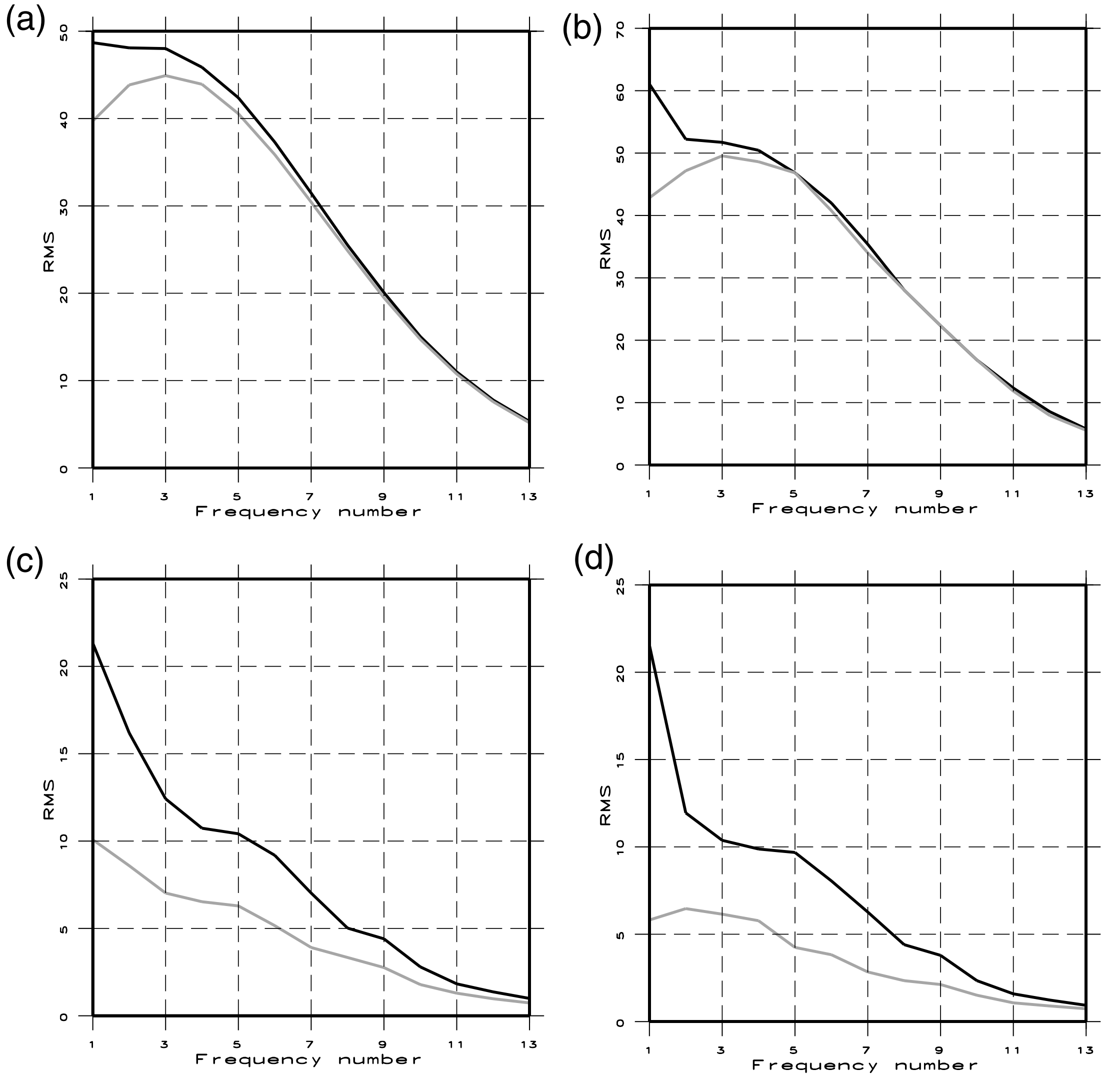

Figure 3. Cost function versus frequency number. The black line represents the cost function corresponding to the starting model (namely, the final model obtained close to inversion of the previous frequency component in the frame of a non-linear iterative inversion) used for the inverted frequency component. The grey line corresponds to the cost function corresponding to the final model of the inverted frequency component. Parts (a–d) show cost functions corresponding to the waveform tomography application of Figs 1(d), (e), (g) and (h) respectively.

Such an integrated analysis will be illustrated with the following real data example.

In order to assess more accurately the impact of errors in the starting model of subsurface velocities we used as a starting model for waveform tomography the smooth model of Fig. 1(b) except that the velocities between 0 and 100 m depth were replaced by the velocities of the overthrust dip section (Fig. 1f). Waveform tomography was performed for known and unknown source excitations (Figs 1g and h). The waveform tomography models of Figs 1(g) and (h) are not polluted by the previous artefacts. Small-scale features such as lenses and channels are clearly observed (at a distance of 14 km and depth of 2.7 km and a distance of 17 km and depth of 0.5 km). Synthetic seismograms computed in the models of Figs 1(g) and (h) are shown in Figs 2(g) and (h) respectively. Note that source estimation surprisingly helped to improve the fit of a refracted wave in Fig. 2(g), suggesting that the source estimation helps to account for small kinematic inaccuracies of the starting model. The cost function plotted with respect to frequency components corresponding to the two applications of Figs 1(g) and (h) is shown in Figs 3(c) and (d).

Waveform tomography images of Figs 1(g) and (h) confirm that quantitative velocity models with high signal-to-noise ratio and broad wavenumber bandwidth can be obtained from sequential waveform inversion of a limited number of realistic frequency components (13 frequencies in the 6–20 Hz frequency band) when wide-aperture acquisition geometry and a kinematically accurate starting model are available. Sequential monofrequency component inversions provide ringing-free tomographic images thanks to the broad wavenumber coverage provided by wide-aperture acquisition geometry.

The quantitative aspect of the waveform tomography can be assessed more accurately in Fig. 4, where two velocity–depth functions located at distances of 4.5 and 13.6 km extracted from the true model, the starting model and the waveform tomography models of Figs 1(d, e) and (g, h) are compared. The log at 13.6 km cross-cuts a channel at 2.5–2.7 km depth. Some underestimations of velocities

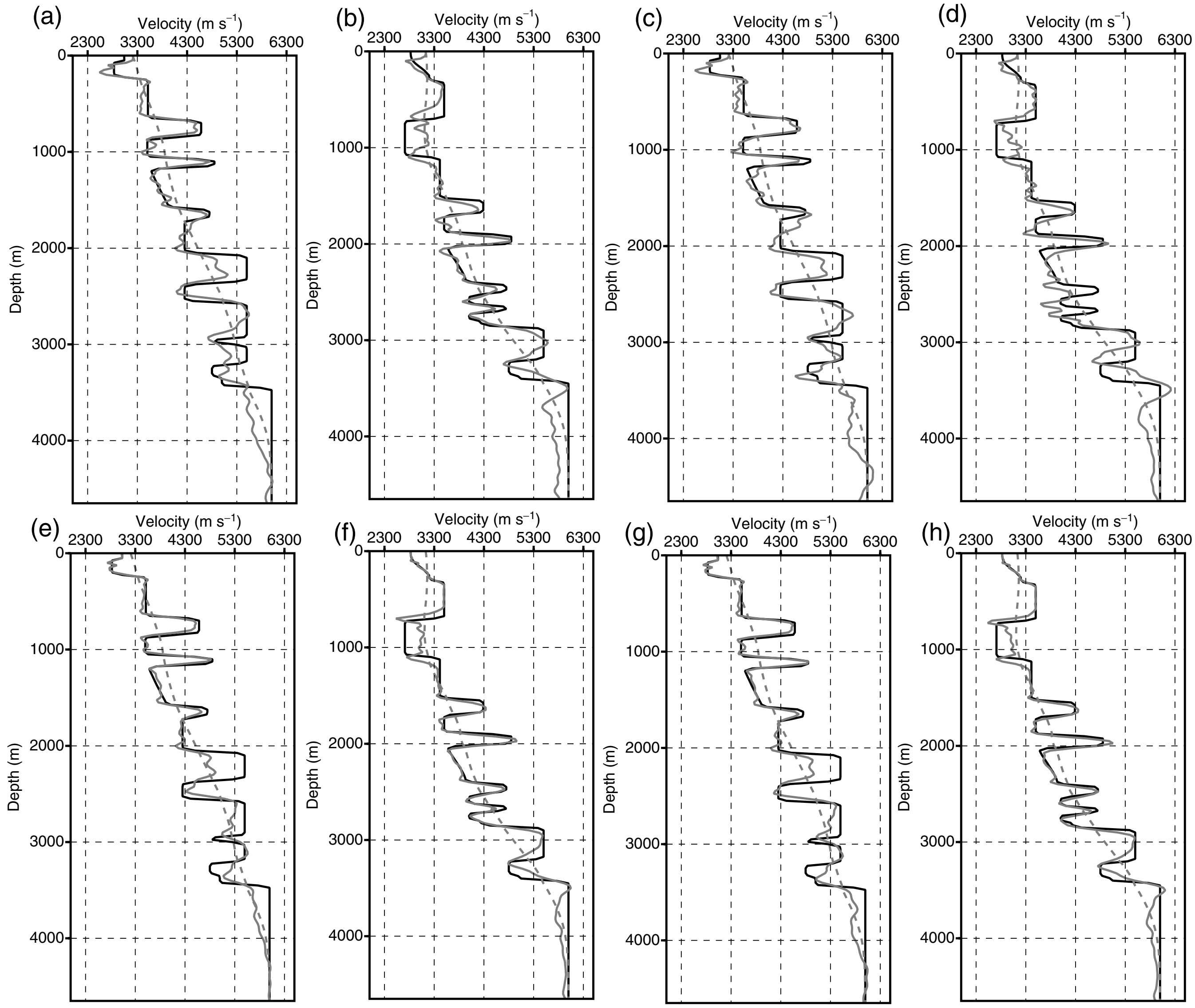

Figure 4. Comparison between velocity–depth functions extracted from the true model (solid black line), the smooth starting model (dashed grey line) and waveform tomography models (solid grey line). In (a) and (b) logs are extracted from the waveform tomography model of Fig. 1(d) at distances of 4.5 and 13.6 km respectively. (c, d) Same as (a, b) for the waveform tomography model of Fig. 1(e). (e, f) Same as (a, b) for the waveform tomography model of Fig. 1(g). (g, h) Same as (a, b) for the waveform tomography model of Fig. 1(h).

and low-wavenumber deficit are observed in the deep part of the model. These inaccuracies result from an insufficient large-offset (i.e. large-aperture) illumination near the ends of the model. Clearly, these failures result from insufficient length of the source/receiver line but not from the waveform tomography itself.

APPLICATION TO REAL DATA

Geological setting

The seismic data processed in this paper have been collected in the axial zone of the Southern Apennines (Italy) thrust and fold belt by the Enterprise Oil Italiana (Fig. 5). The investigated area is characterized by a strongly heterogeneous crustal structure.

The geological setting consists of a tectonic stack of northeast-verging sheets involving Jurassic rocks (cherty dolomites, cherts) and Cretaceous shales. These basinal units are overthrusted by a regional nappe, which consists of a tectonic melange of Palaeocene clays and marly limestones (Fig. 5a). The shallower units include Pliocene soft sediments representing the infill of small basins. The main surface tectonic structures crossed by the seismic profile are a northwest-trending synform, filled by soft Pliocene sediments, and broad nappe anticline, the latter responsible for a tectonic window where Mesozoic rocks crop out.

Due to the presence of clayey strata alternated with Mesozoic hard-rock sheets, and to a variable surface geology, strong lateral variations and velocity inversions are present at all depths. The heterogeneous velocity structure, along with a rough topography (Fig. 5b) hamper the collection of good-quality near-vertical reflection data, which are otherwise affected by strong diffractions, multiples, surface waves and static problems. In addition, in such a context, standard velocity analysis is inadequate to estimate accurate background velocity models for pre-stack migration/inversion. As a consequence, multichannel reflection seismograms usually yield

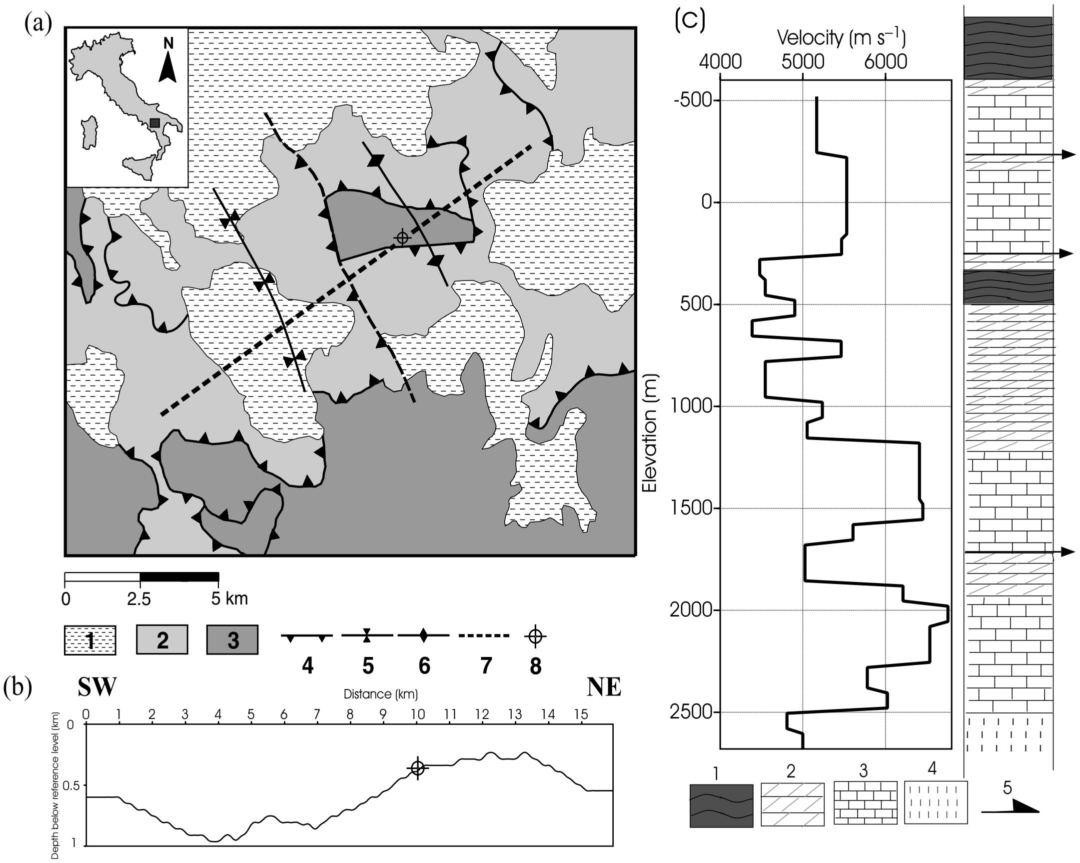

Figure 5. (a) Tectonic setting in the target area: 1, Plio-Pleistocene soft sediments; 2, Palaeocene clayey and marly calcareous tectonic melange; 3, Mesozoic basinal rocks; 4, thrust; 5, syncline; 6, anticline; 7, seismic profile; 8, well for oil exploration. (b) Topography along the seismic profile. The position of the well along the profile is indicated. (c) Velocity–depth and petrological profiles determined by VSP data: 1, shales (Lower Cretaceous); 2, cherts (Jurassic–Upper Triassic); 3, Cherty limestones (Upper Triassic); 4, sandstones (Middle–Lower Triassic); 5, main thrust planes (from Improta *et al.* 2002).

only poor-quality structural images in the investigated area (Fig. 6). In order to address this problem, alternative geophysical exploration tools (multifold wide-angle seismograms, well-logging (Fig. 5c), magnetotelluric and gravity measurements) have been jointly used in the region (Dell'Aversana 2001).

Acquisition geometry

The 2-D acquisition geometry consists of a southwest–northeast line, 14 200 m long, running above a synform and a wide antiform. The profile strikes northeast–southwest and is almost perpendicular to the main thrust front and fold axes in the area. The profile is tied to a deep well drilled in the core of the antiform (Fig. 5a). The topography along the profile is rough. The maximum difference in altitude between sources reaches 700 m (Fig. 5b). The surface receiver array consists of 160 vertical geophones deployed along the 2-D line with a 90 m interval. Two hundred and thirty-three shots were fired with an average spacing of 60 m into the array by housing explosive charges in boreholes 30 m deep (for a detailed description of the experiment design see Dell'Aversana *et al.* 2000). This acquisition geometry leads to a multifold wide-aperture acquisition with densely sampled source and receiver spacings amenable to full-waveform inversion.

Data quality

A representative example of common receiver gather (CRG) is presented in Fig. 7. In Fig. 7(a) the CRG was bandpass filtered in the 4–50 Hz band. Note the sharp amplitude variations with offset which may result from factors other than elastic wave propagation (e.g. attenuation, shot size variability, receiver–ground coupling, subsurface weathering). One can intuitively anticipate that such data cannot be directly incorporated in the waveform tomography program but require some specific pre-processing since wavefields are affected by many factors that are not accounted for in the wave modelling and inversion algorithms.

In order to perform a qualitative interpretation of wavefields, the CRG shown in Fig. 7(b) have been processed by minimum phase whitening, Butterworth bandpass filtering and automatic gain control (AGC). Refracted waves, Re, and two wide-angle reflections, R1 and R2, are labelled in Fig. 7(b). Note also the sharp attenuation of the refracted wave at offsets greater than 5 km indicating the presence of a possible low-velocity zone (SZ). The amplitude spectra of the bandpass-filtered data, the data after minimum phase whitening and the data after minimum phase whitening and Butterworth band-pass filtering are shown in the inset of Fig. 7(a).

The starting model

Application of the non-linear traveltime tomography to the data set used in this paper has already been presented in Improta *et al.* (2002). The velocity model used as a starting model for waveform tomography is shown in Fig. 8(a). Over 6000 first-arrival traveltimes, from 32 receivers, have been inverted. The velocity model that we used as the starting model for the waveform tomography (Fig. 8a)

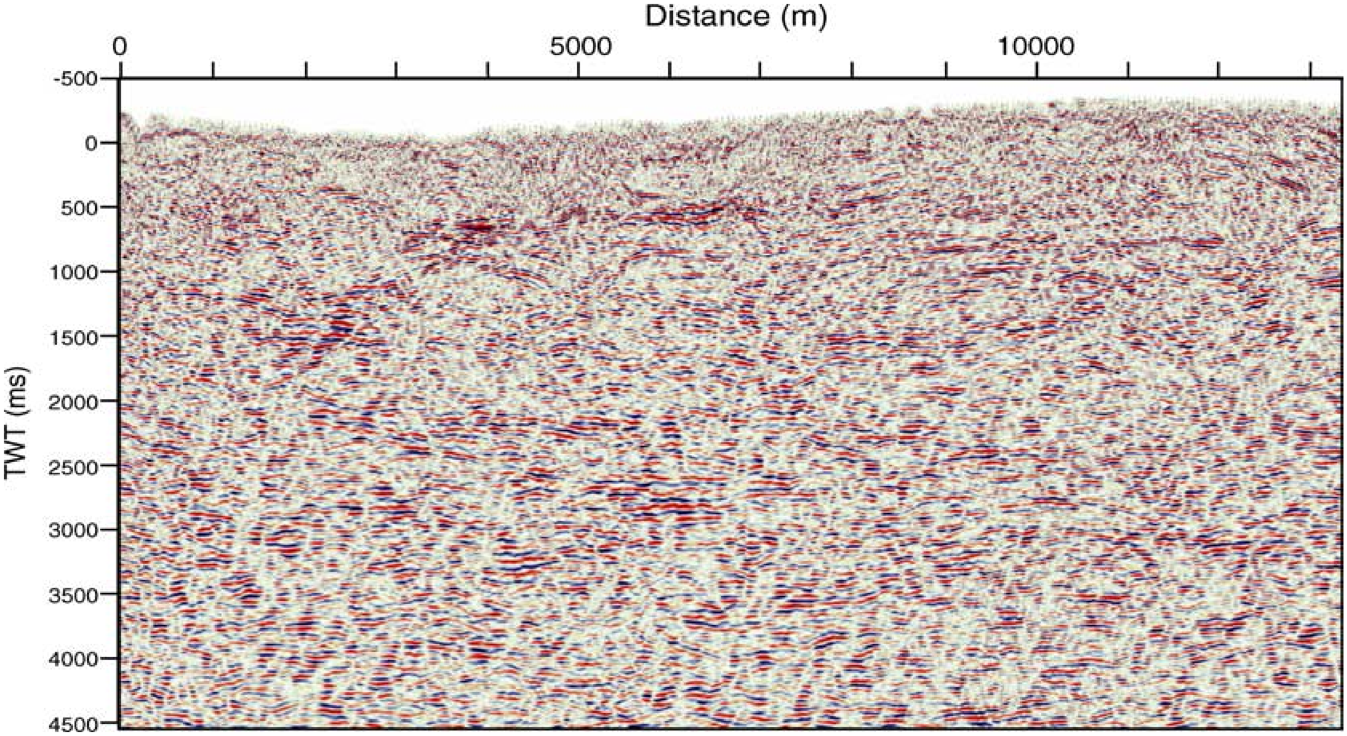

Figure 6. Time-migrated stack section obtained by conventional processing of seismic multichannel reflection data collected along the investigated wide-aperture profile. The horizontal axis is labelled between 0 and 13 km distance with the same coordinate system as the one used for the wide-aperture profile. Note the overall poor quality of the data and the low reflectivity on the right-hand side of the section beneath the antiform.

was obtained after four inversion runs and was parametrized during the last run (which involves the finer parametrization) by 128 spline nodes (16 and eight nodes horizontally and vertically respectively). Checkboarder resolution tests indicated that the model is well resolved down to about 1.6–1.8 km depth in the 4–12 km distance range. Velocities range between 2.0 and 7.0 km s^{-1}. The traveltime tomographic velocity model was subsequently interpolated on a 639 × 171 regular grid with a 25 m grid interval. This discretization was used to solve the forward-modelling problem in the waveform tomography program. Since the finite-difference stencils implemented in the wave modelling program require four points per minimum wavelength, the maximum frequency that was involved in the waveform tomography was 20 Hz.

The linearized waveform tomography requires that the first-arrival times are matched to within a half-cycle associated with the frequency component to be inverted to avoid cycle-skipping artefacts in the inversion. The superposition of the first arrival times on the CRG of Fig. 8 suggests that this condition is reasonably verified for the dominant frequency of the source bandwidth (and hence for the lower frequency processed by waveform tomography) when using the velocity model of Figs 8(b)–(c).

Waveform tomography data pre-processing

Successful application of waveform tomography requires the design of a specific pre-processing of the data. The objectives of the pre-processing are

(1) Improvement of signal-to-noise ratio.

(2) Mitigation of several amplitude variations which are difficult or impossible to incorporate accurately in the wave modelling routines. Among the potential factors which control the amplitude behaviour apart from the elastic properties of the propagation medium, we noted the variability of the source size from one shot to the next, the variability of the receiver–ground coupling, the source directivity and attenuation. The source energy and directivity are difficult to account for because their direct measurement during the acquisition is not straightforward. Ground–receiver coupling is controlled by the near-surface properties which may not be known precisely. Moreover, the uniform grid parametrization of the finite-difference wave modelling routine used in this study does not allow us to represent these near-surface properties accurately enough. As mentioned before, attenuation can be easily implemented in the modelling routine through the use of complex velocities. Inversion for the attenuation factor Q can also be envisaged although the construction of a starting Q model and the assessment of the reliability of the Q images will probably not be straightforward. At the present stage, incorporation of attenuation effects is not considered in our approach.

(3) Removal of arrivals which are not predicted by the approximation used to represent the physics of acoustic wave modelling or which do not carry any geological information. These arrivals are essentially P- to S-mode converted waves and surface waves (i.e. ground rolls).

The pre-processing sequence contains the following tasks:

(1) Minimum-phase whitening including a normalization of the amplitude spectrum of each trace with respect to its maximum.

(2) Butterworth band-pass filtering to improve the signal-to-noise ratio.

(3) Quality control and trace editing to remove noisy traces.

(4) Application of a reduced timescale to facilitate subsequent application of coherency filtering.

(5) Coherency filtering using spectral matrix filtering (Glangeaud & Coppens 1997) to improve the signal-to-noise ratio and to strengthen the lateral trace coherency. This processing

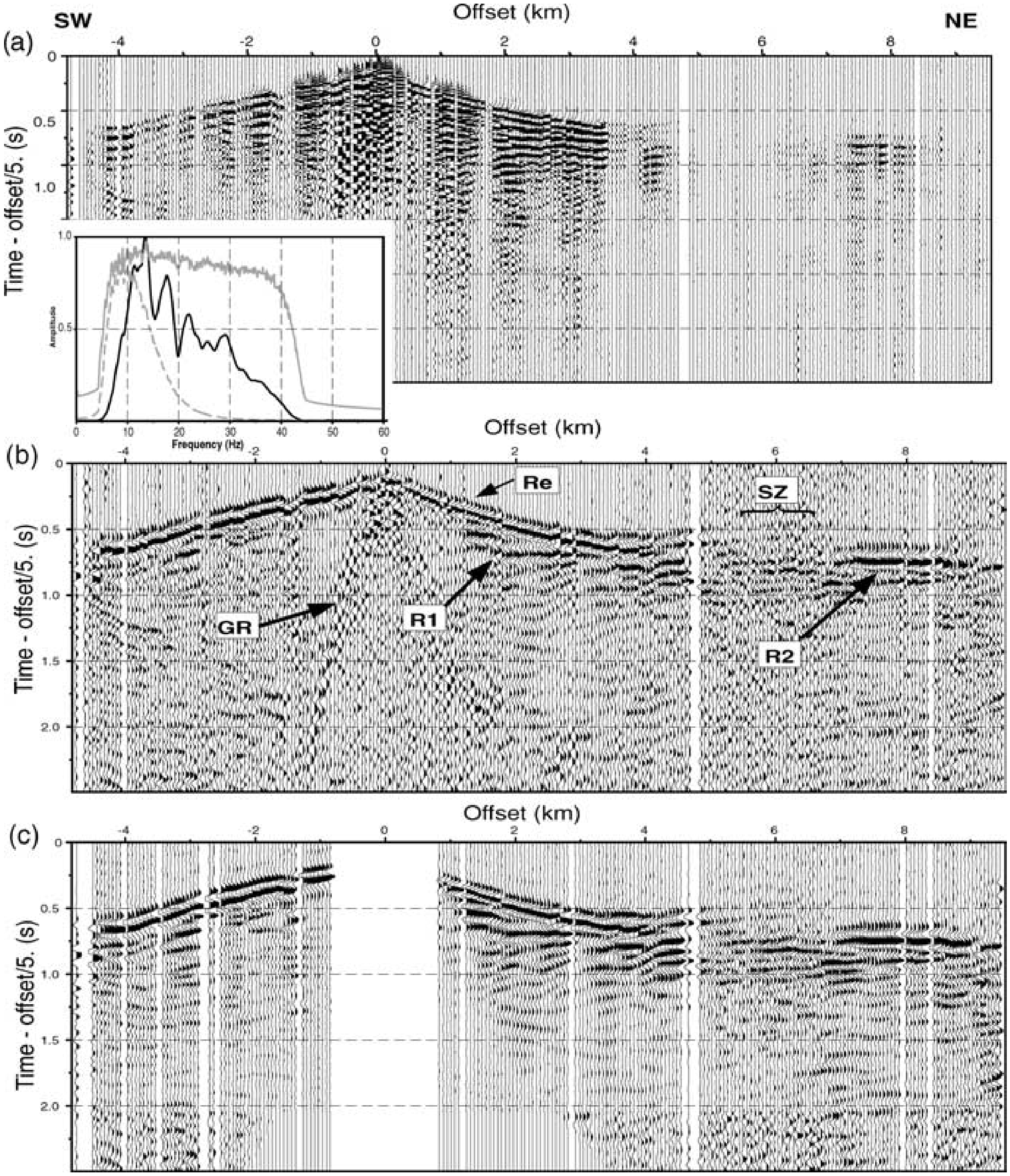

Figure 7. Example of a common receiver gather. The receiver is located at $x = 5.75$ km in Fig. 5(b). (a) The CRG was processed by Butterworth bandpass filtering with cut-off frequencies of 4 and 50 Hz. (b) The CRG was processed by minimum phase whitening, Butterworth filtering and automatic gain control. The main arrivals are labelled: Re, refracted waves: GR, ground rolls; R1 and R2 wide-angle reflections; SZ, shadow zone. A reduced timescale is applied with a reduction velocity of 5 km s^{-1}. (c) The CRG of part (a) after waveform inversion data pre-processing. The inset to (a) shows the amplitude spectrum of the CRG of the main figure (a) (black curve), of the CRG after whitening only (solid grey line) and of the CRG of Fig. 7(c).

is based on the projection of the signal on the main eigenvectors of the frequency-domain cross-correlation matrices. This projection separates the coherent signal from uncorrelated noise.

(6) Offset and time windowing. The traces within the 0–0.8 km offset range were removed to eliminate ground rolls. Time windowing was applied to eliminate late arrivals which correspond to deep reflections coming from outside the limits of our model and *P*–*S* converted waves.

The CRG of Fig. 7(a) after the waveform tomography pre-processing is shown in Fig. 7(c). The effect of the whitening is to normalize spectral amplitude and to flatten it in the frequency bandwidth of the source (Fig. 7a). The amplitude normalization should partially compensate for the effects of the source size variability, the receiver–ground coupling and attenuation. Flattening of the spectrum may help to compensate for the effect of the source directivity. Spectral amplitude normalization weights the data such that each trace in the waveform tomography has a similar contribution and implies that the amplitude versus offset information is not preserved. The amplitude versus offset information was not preserved because it was considered to be affected by too many factors to be exploited confidently. However, amplitude variations are fully

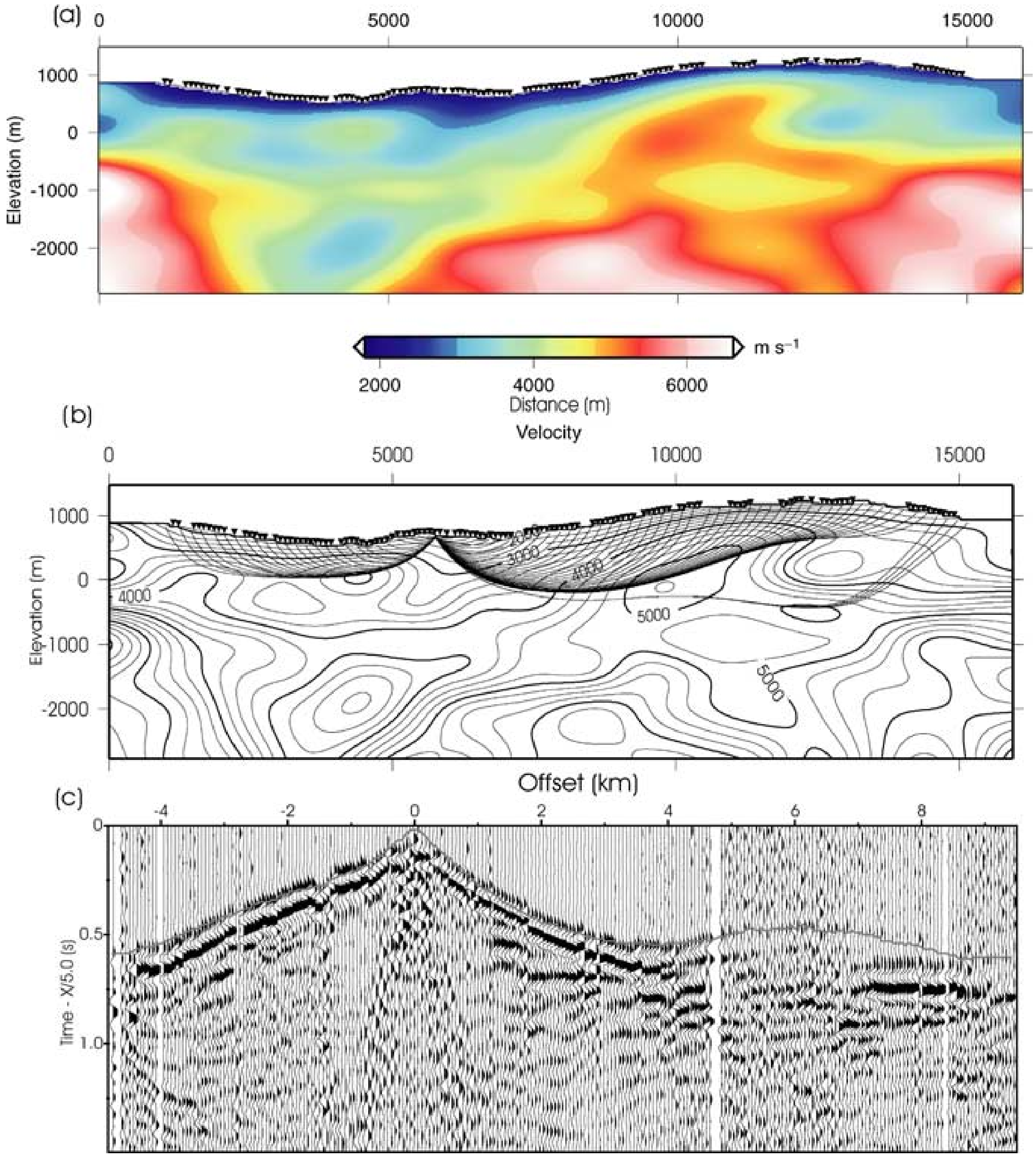

Figure 8. (a) Starting velocity model for full-waveform tomography. The triangles show the position of the receivers that were involved in the full-waveform inversion. (b) Ray tracing in the velocity model of part (a). The rays are traced from the receiver position given by $x = 5.75$ km. (c) First-arrival traveltimes are superimposed on the CRG shown in Fig. 7.

preserved along the time axis and our intuition tells us that this information is enough to properly recover the *P*-wave velocities in the frame of a monoparameter waveform tomography.

The acoustic wave equation (eq. 4) provides the pressure wavefield. The vertical geophone measures vertical particle velocity. Rigorously, a conversion from pressure to vertical particle velocity would be required in the finite-difference forward-modelling code before fitting the observed velocity and the computed pressure wavefields.

In the temporal frequency domain, the relation between the vertical displacement velocity and the pressure field is given by

$$-i\omega\rho v_z = \frac{\partial P}{\partial z} \tag{12}$$

where ρ is density and v_z is the displacement velocity. Then, the pressure–velocity conversion would require to compute by finite difference the spatial derivative of the pressure field with respect to the vertical axis and to divide the resultant signal by $-i\omega$. Moreover, if the pressure-to-vertical particle velocity conversion is applied, the Jacobian matrix of the partial derivative of pressure data with respect to model parameter in eq. (6) must be replaced by that of the partial derivative of vertical particle velocity with respect to model parameter.

At present we don't make any attempt to explicitly apply such a conversion. We rather apply some empirical amplitude weighting to the observed data such that the weighted vertical geophone data mimic pressure data. The waveform shape of the pressure and vertical velocity fields are essentially related by a derivative relation, eq. (12) and p. 225 of Sheriff & Geldart (1995). This relation can be accounted for by the source term *o* which is embedded in the waveform tomography algorithm, eq. (11). The amplitude-versus-angle behaviour of the pressure and vertical velocity fields are rather

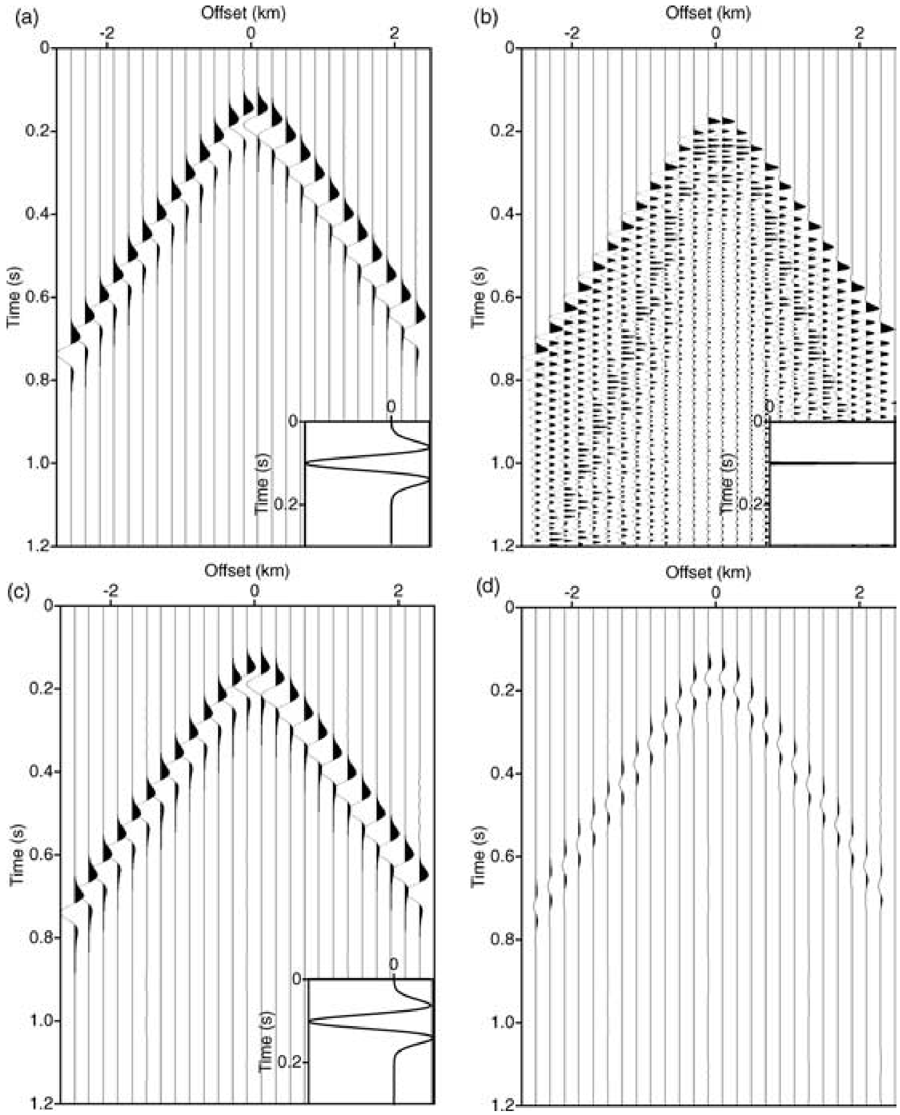

Figure 9. (a) Vertical particle velocity seismograms computed in a homogeneous medium for the source signature shown on the bottom right. The receivers are on the surface. The source is located in the middle of the receiver array just below the receiver line. Each trace have been normalized by its maximum amplitude. These seismograms are treated as observations in the frame of this synthetic experiment. (b) Pressure seismograms computed in the same homogeneous medium for an impulsional source excitation (shown on the bottom right). The seismograms exhibit numerical dispersion due to the infinite bandwidth of the source function. (c) Pressure field obtained by convolution of the impulsional seismograms of part (b) with the source function shown on the bottom right. Each trace has been normalized by its maximum amplitude. The source signature has been estimated such that the difference between the normalized vertical particle velocity seismograms in (a) and the normalized pressure seismograms in (c) is minimized in a least-squares sense, eq. (11). (d) Difference between the seismograms of parts (a) and (c). The weak amplitude of the residuals shows that pressure seismograms can mimic vertical particle velocity seismograms under the condition that seismograms are normalized by their maximum amplitude.

different since the amplitude of the vertical velocity is sensitive to the incidence angle of the arrival at the sensor. This makes the match between the observed vertical particle velocity and the computed pressure fields to be ill-founded if no amplitude scaling is applied to observed data. We used the spectral amplitude normalization applied by the whitening to weight the amplitude-versus-angle behaviour of vertical particle velocity seismograms. Fig. 9 suggests that, after trace amplitude normalization, a source function o (eq. 11) can be found such that the pressure scalar equation could match properly the normalized vertical particle velocity field.

The last point concerns the fact that the waveform modelling and inversion are 2-D while the observed data experience 3-D propagation. An approximate 3-D to 2-D conversion of the observed data can be applied through convolution with a filter of the form $\mathcal{H}(t)/\sqrt{\pi t}$ (Williamson & Pratt 1995). This filter mainly increases low-frequency components in the amplitude spectrum. Nevertheless, this approximation is only valid for a quasi-tabular medium. After band-pass filtering within the frequency bandwidth of the source, the effect of the 3-D to 2-D conversion is significantly mitigated. Therefore, we have not applied any 3-D to 2-D conversion considering that this correction affects essentially the low-frequency part of the data which is outside the source bandwidth. The synthetic simulation shown in Fig. 10 illustrates this point and suggests that this assumption is reasonable.

Note also a difficulty associated with frequency-domain waveform tomography. For consistency, the same pre-processings should be applied to the observed and computed data to calculate the misfit before waveform tomography (Chapman & Orcutt 1985). Some of

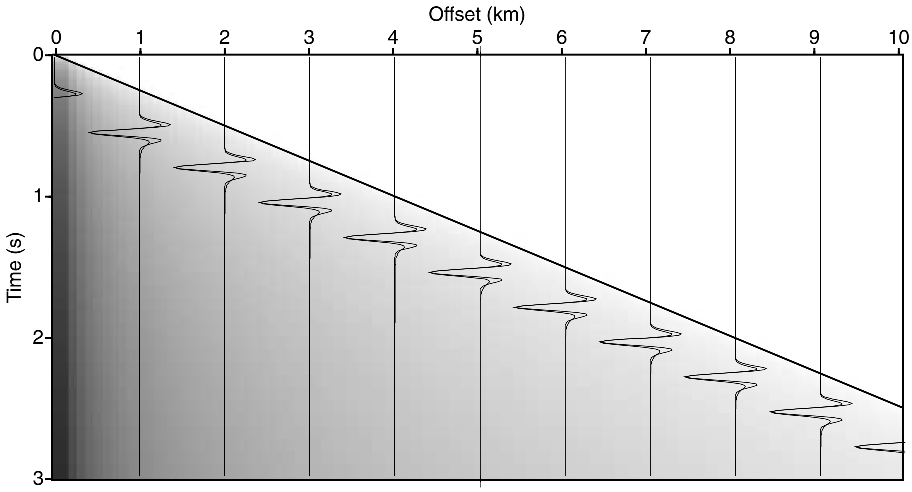

Figure 10. Comparison between 2-D and 3-D seismograms for a source bandwidth characteristic of a crustal-scale seismic experiment. The grey area represents 2-D impulsional seismograms (i.e. computed for a source with an infinite bandwidth) exhibiting the typical 2-D tail. The solid line symbolizes 3-D impulsional seismograms formed by a series of delayed delta functions. The fit between 2-D (black seismograms) and 3-D (grey seismograms) band-limited seismograms is reasonably good.

the pre-processings applied to the observed data are performed in the time domain (time windowing) or require us to know the amplitude of each frequency component at a time. For example, the whitening is regularized by a pre-whitening factor which is added to the amplitude of the deconvolution operator to avoid division by zero. This pre-whitening factor is defined as a percentage of the spectral amplitude maximum. Computation of this maximum requires us to know all the frequency components of the trace at a time.

Since frequency-domain waveform modelling and tomography process one frequency component at a time, it is not possible to our knowledge to rigorously apply to the computed monochromatic synthetics the specific waveform pre-processings which require the knowledge of all the frequency components.

The goal of time windowing was essentially to remove later-arriving phases which are not predicted by the acoustic approximation. Hence, the fact that time windowing cannot be applied to the computed data is unlikely to remove significant energy from the computed seismograms.

The fact that whitening was not applied to the computed data is more conceptually questionable. At present we were unable to design an efficient data weighting which can be applied in the same manner to the observed and computed data. We assumed that the observed seismograms after whitening plus normalization reflect the amplitude versus offset behaviour of acoustic synthetic seismograms. Although this approximation may appear crude, we have obtained waveform tomography images which revealed geological features whose relevance was demonstrated.

Waveform tomography results

The best waveform tomography models that we obtained are depicted at different stages (i.e. resolution) of the imaging process in Fig. 11. The waveform tomography velocity models were kept unperturbed between the depths of 0 and 100 m during inversion to avoid near-surface instabilities (see results of the overthrust experiment). One hundred and nineteen CRGs were selected for waveform tomography among the 160 available gathers. Their positions along the profile are given in Fig. 11. This data set represents 20 563 traces. Sixteen frequency components ranging from 5.4 to 20 Hz were inverted sequentially. Although the data have a higher frequency content, we didn't make any attempt to invert frequency components greater than 20 Hz. Inversion of the highest frequency components would theoretically allow us to improve the spatial resolution of the waveform tomography images. Nevertheless, waveform modelling of frequencies higher than 20 Hz would have required us to make the finite-difference grid smaller, leading to an increase of the necessary computational resources (both in terms of memory and computational time). Moreover, waveform tomography becomes more non-linear at high frequencies and the cost-function minimization became less and less effective at frequencies greater than 15 Hz. For these two reasons, we decided to stop the waveform tomography at a frequency of 20 Hz.

The interval between inverted frequency components was around 1 Hz. This frequency interval was chosen heuristically to reach a reasonable trade-off between the need to decimate data redundancy in the wavenumber domain to limit the number of frequencies to be inverted (Sirgue & Pratt 2001), and hence saving CPU time, and the need to stack redundant data to improve the signal-to-noise ratio.

Twice as many frequency components (i.e. 32 frequency components) were also inverted within the same frequency range without significant improvement of the velocity models.

Ten iterations were computed per frequency component. No rigorous criteria were used to define an optimal number of iterations. We found that 10 iterations was the best trade-off between the need to lower the cost function as much as possible and the computational cost.

For all the inversions, model parameters were discretized on a Cartesian grid with a grid interval of 100 m horizontally and 25 m vertically. This corresponds to $\mathrm{decim}_x = 4$ and $\mathrm{decim}_z = 1$ given that the grid interval for the forward modelling was 25 m (see section entitled Frequency-domain full-waveform tomography).

The input parameters for waveform inversion that allowed us to obtain the velocity models of Fig. 11 are summarized in Table 1.

The velocity models shown in Fig. 11 were obtained close to the inversion of the frequency components 5.38, 10.27, 15.16 and 20 Hz respectively. Note how the waveform tomography incorporates details of the structure in the velocity models as the inversion progresses towards high frequencies. The most noticeable structures

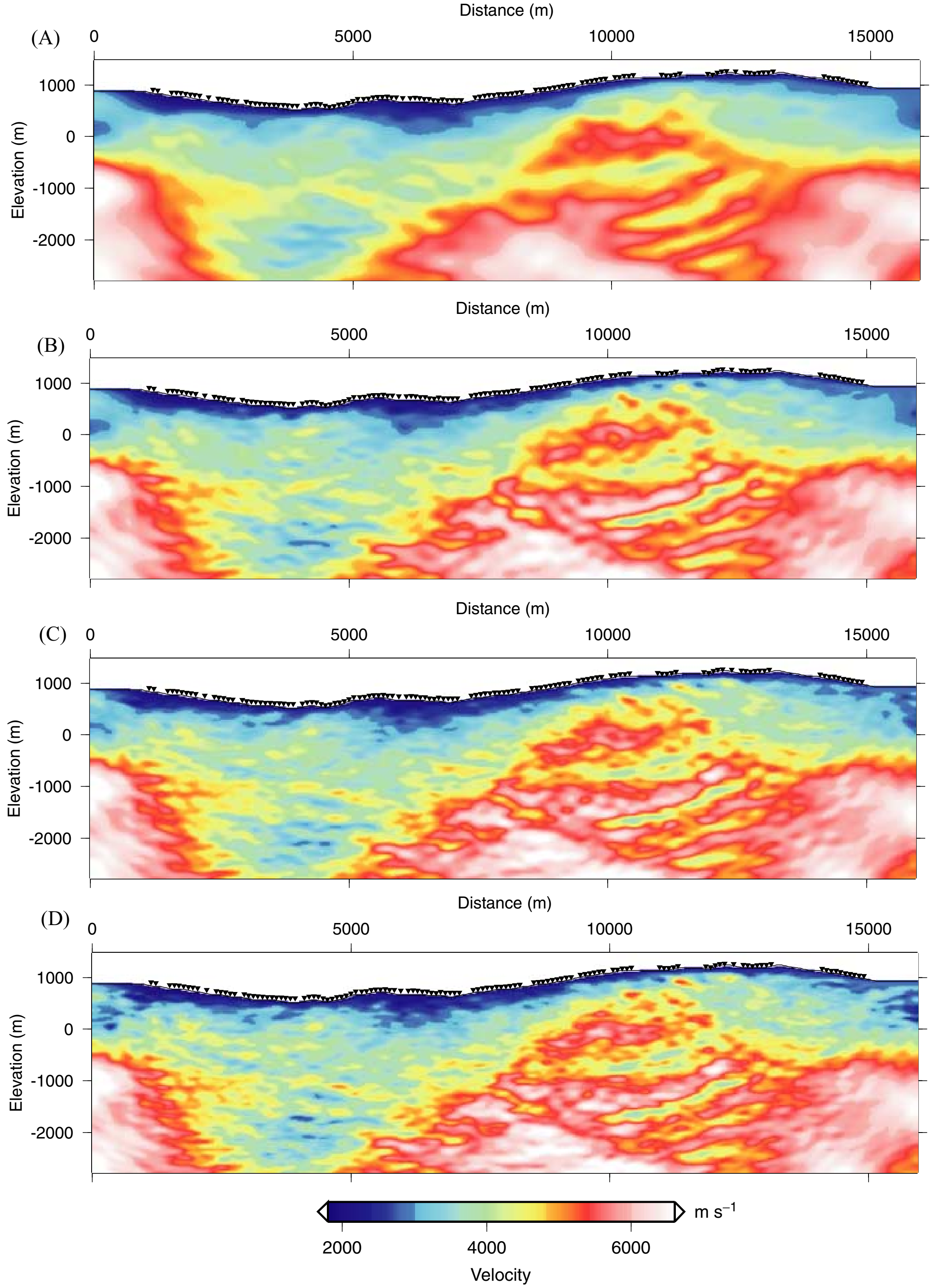

Figure 11. Velocity models from full-waveform tomography using $\epsilon = 2 \times 10^{-3}$ close to inversion of the 5.38 Hz (a), 10.27 Hz (b), 15.16 Hz (c) and 20.06 Hz (d) frequencies components respectively.

are high-velocity southwest-dipping slices at around $x = 10$ km and $z = 1$–2 km in Figs 11(a)–(d) corresponding to high-resistivity bodies previously identified by Dell'Aversana (2001). Note that the inversion of a rather low-frequency component such as 5.38 Hz already incorporates these southwest-dipping structures in the velocity models (Fig. 11a).

The pre-conditioning of the gradient is shown in Fig. 12. Fig. 12 maps the diagonal terms of the approximate Hessian matrix, which is the resolution operator (Lambaré *et al.* 2003). The gradient was weighted by this map. One can see how the shallow perturbations are penalized by this pre-conditioning with respect to the deep perturbations due to the surface acquisition geometry. The

Table 1. Input parameters for waveform inversion: h, grid interval of the finite-difference grid used for forward modelling; h_x and h_z, grid intervals for the velocity grid involved in the waveform inversion; ϵ, regularization of the gradient pre-conditioning; p_x, p_z and c_0, parameters defining the smoothing operator applied to the gradient (see text); N_υ, number of inverted frequencies; $\Delta\upsilon$, frequency interval; N_{it}, number of iterations per frequency; υ_{min}, smallest inverted frequency; υ_{max}, highest inverted frequency.

Parameter	Value
h (m)	25
h_x (m)	100
h_z (m)	25
ϵ	0.002
p_x	0.3
p_z	0.1
c_0 (m s^{-1})	3000
N_υ	16
$\Delta\upsilon$ (Hz)	1
N_{it}/υ	10
υ_{min} (Hz)	5.56
υ_{max} (Hz)	20

regularization parameter ϵ in eq. (9) is used to avoid instabilities resulting from non-uniform illumination of the medium and mitigates the effect of this weighting in a comparable way to a pre-whitening factor in a predictive deconvolution processing. Due to the surface acquisition, this implies that increasing the ϵ parameter penalizes the deep perturbations with respect to the shallow ones.

The models shown in Fig. 11 were obtained with $\epsilon = 0.002$. It is helpful to benefit locally from independent information on the velocity–depth structure (e.g. *a priori* geological knowledge of the target, well log) to choose the optimal value for this parameter ϵ. For this study, we used a VSP log located at $x = 10$ km (Fig. 5c).

Comparisons between the VSP log and the velocity logs extracted from the traveltime (Fig. 8a) and waveform (Fig. 11) tomography models are shown in Fig. 13. The waveform inversion logs of Figs 13(a–d) were extracted from the models of Figs 11(a–d) respectively. The VSP log in Figs 13(a)–(d) has been low-pass filtered in the time domain in order to fit roughly the expected resolution of the waveform tomography.

One of the main features that was approximately recovered by the waveform tomography is the high-velocity layer centred on $z = 0$ km (Fig. 13d). The high-velocity layer drilled between 1.2 and 1.6 km is also approximately recovered (Figs 13c and d). The arrivals labelled R2 in Fig. 7(b) are probably reflections from this carbonate layer. As documented by the VSP log, these two high-velocity layers are separated from 0.3 km down to 1.2 km by a low-velocity zone in a large-scale sense. This low-velocity zone corresponds to a stack of thin layers of cherts and shales and is probably responsible for the shadow zone observed in data and labelled SZ (Fig. 7b). The waveform tomography identifies each of these thin layers, although the amplitude of the velocity is not well recovered (Fig. 13d). Note that a deep low-velocity cherty layer drilled between 1.6 and 1.9 km is also marked in the waveform tomography log (Fig. 13d). Finally, a sharp velocity increase at 1.9 km in the waveform tomography log matches the top of the high-velocity dolomite layer drilled between 1.9 and 2.5 km.

Fig. 14 presents waveform tomography models for a higher and lower regularization parameter ϵ ($\epsilon = 0.005$ and $\epsilon = 0.001$). One can note the expected effect of this parameter on the amplitude of velocities with depth. The comparison between the velocity logs extracted from the models of Fig. 14 with the traveltime tomography and VSP logs is shown in Fig. 15.

The velocity amplitude calibration is also reasonably good for $\epsilon = 0.005$, although a slight underestimation of velocities is observed in the deeper part of the model with respect to the VSP log (Fig. 15a). The velocity log obtained with $\epsilon = 0.005$ is close to that obtained with $\epsilon = 0.002$ (compare Figs 13d and 15a), suggesting that the waveform tomography is properly regularized for this range of ϵ values. The velocity log in Fig. 15(b) ($\epsilon = 0.001$) exhibits more oscillations suggesting less stable inversion for this rather low value of the regularization parameter ϵ.

The RMS misfit as a function of the frequency and the iteration number is shown in Fig. 16. At a maximum, a reduction of the cost function of only 10 per cent was obtained. This was obtained for the dominant frequency component of the source spectrum (9 Hz). The misfit reduction is comparable to that obtained in the frame of the synthetic overthrust experiment when the velocity structure is kept fixed between 0 and 100 m depth (see Figs 1d, e, 2c, e, 3a, b and

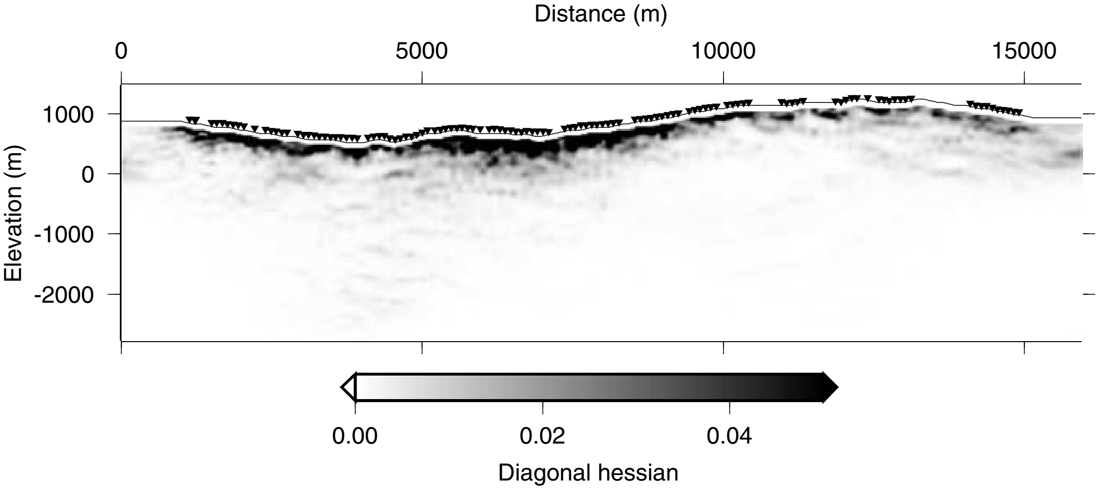

Figure 12. Gradient pre-conditioning formed by the diagonal elements of the Hessian.

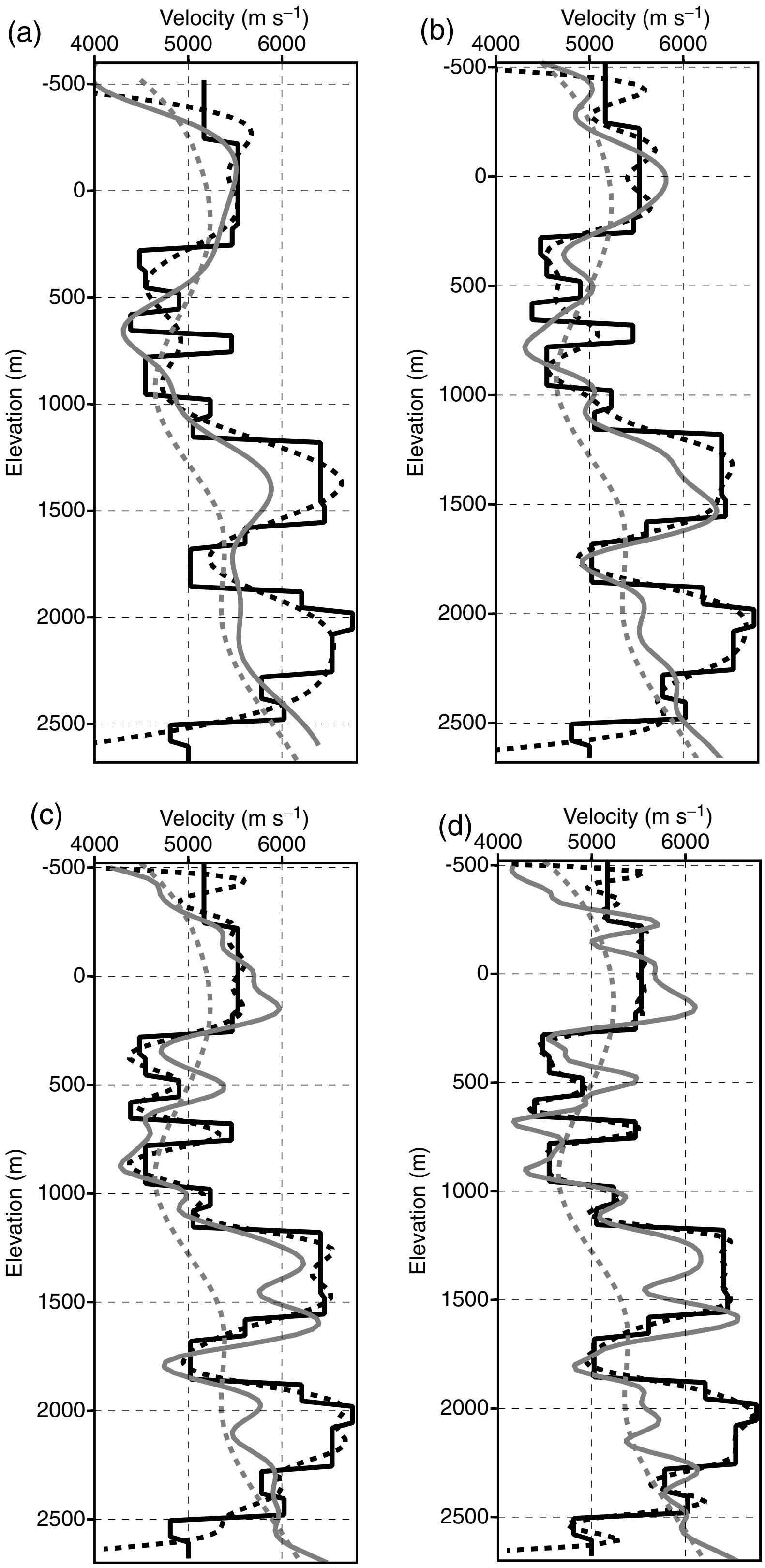

Figure 13. Comparison between VSP and traveltime and waveform tomography velocity logs: VSP log (solid black line), low-pass filtered VSP log (dotted black line), traveltime tomography log (dotted grey line), waveform tomography log (solid grey line). The waveform tomography logs of (a)–(d) have been extracted from the velocity models of Figs 11(a)–(d) respectively.

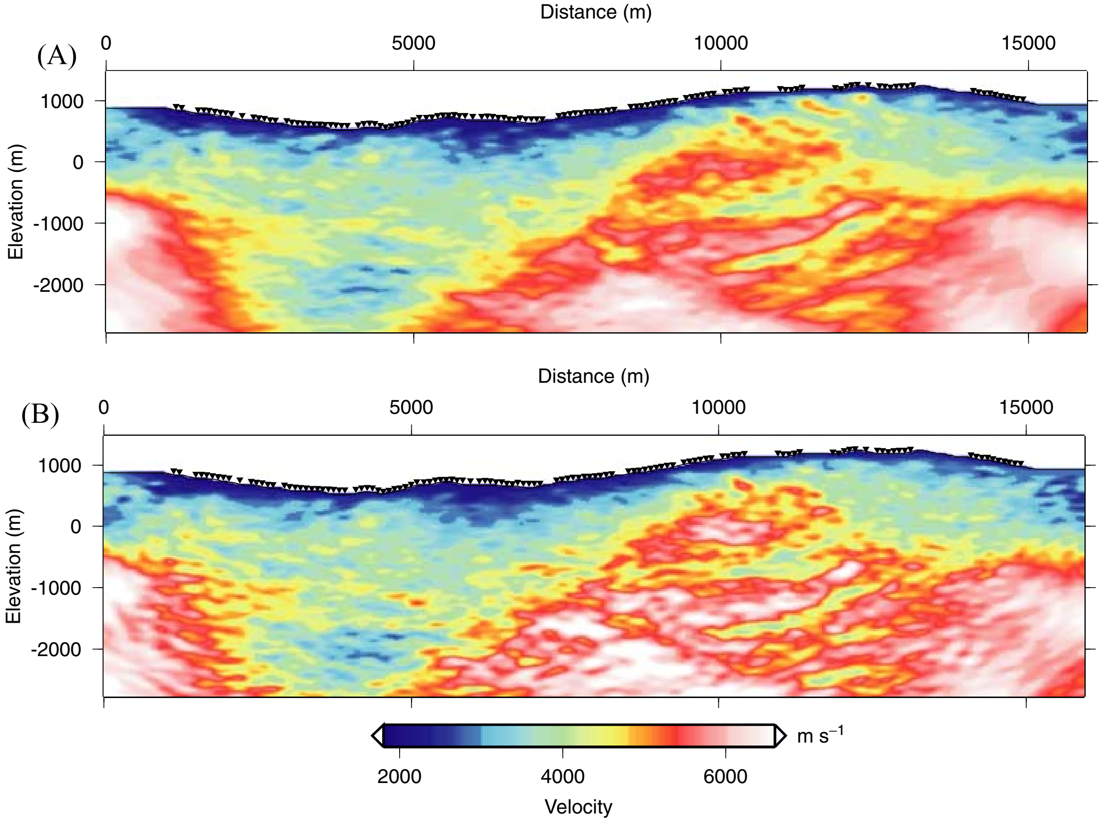

Figure 14. Velocity models from full-waveform tomography using (a) $\epsilon = 5 \times 10^{-3}$ and (b) $\epsilon = 1 \times 10^{-3}$ close to inversion of the 20.06 Hz frequency.

4a–d to assess the relationship between the quality of the waveform tomography images and the amount of misfit reduction).

This poor fit of the data may partly result from: (1) velocity inaccuracies in the subsurface of the waveform tomography model (see results of the overthrust synthetic test); (2) approximations that we made in the waveform modelling and inversion (see section entitled Waveform inversion data pre-processing); (3) inconsistencies between the amplitude versus offset behaviour of the observed data after whitening and the computed data which make difficult the fit of the amplitude spectra of the data in the full offset range. For information, inversion of only one CRG allows us to reach a reduction of the cost function of the order of 50 per cent.

In order to assess qualitatively which part of the data contributed significantly to the model reconstruction we compute time-domain finite-difference (FDTD) seismograms in the traveltime and waveform tomography velocity models (Fig. 17). The source that was used for this simulation is located at the position of the receiver of the CRG of Fig. 7. We used a bandpass-filtered delta function for the temporal source function which should provide a good approximation of source excitation to model whitened and bandpass-filtered data. Direct comparison between the data of Fig. 7(c) and seismograms computed in the traveltime and waveform tomography models of Figs 11(b), (c) and (d) is shown in the right panels of Figs 17(b)–(e). Each seismogram has been normalized by its maximum amplitude to facilitate the phase identifications. Moreover, the observed seismograms have been bandpass filtered in a narrow frequency range (cut-off frequencies: 6–10 Hz). Indeed, we observed that the bandwidth of the FDTD seismograms was narrower than that of the source function input in the finite-difference code. This suggests that high frequencies were filtered out during their propagation in the waveform tomography models. We interpret this as the result of extrinsic (scattering) attenuation generated by diffracting structures resulting from poor focalization during the waveform tomography.

In Fig. 17(b) one can note that the first arrival (refracted arrival) is generally correctly predicted by the traveltime tomography model although amplitudes are overestimated in the 5–8 km offset range where the shadow zone was noticed (compare Figs 17a and b). On the contrary the wide-angle reflections R1 and R2 are poorly predicted by the smooth traveltime tomography model. The large-scale high-velocity variation of the traveltime tomography model centred at 1500 m depth (Fig. 13) generates small-amplitude wavefield focusing at large offsets (8–9.5 km) which approximately fits the traveltimes of the R2 wide-angle reflection (Fig. 17b). This wavefield focusing evolves towards a high-amplitude wide-angle reflection spanning a broader range of offsets as waveform tomography incorporates higher wavenumbers in the tomography images (Figs 17c–e). Note also the appearance of the shadow zone corresponding to attenuation of the first-arrival refracted wave while the wide-angle reflection R2 is built (Figs 17c–e). The wide-angle reflection R1 is well predicted in Figs 17(c) and (d) but its match has been degraded close to inversion of the 20 Hz frequency component (Fig. 17e). This suggests that waveform tomography was unstable between 15 and 20 Hz although a close comparison between the logs of Figs 13(c) and (d) proves that at least around the VSP log location the vertical resolution of the waveform tomography images has still been improved up to the 20 Hz frequency component inversion.

Another view of the data fit is illustrated in Fig. 18. A similar data display is used in Pratt (1999); Pratt & Shipp (1999). The full

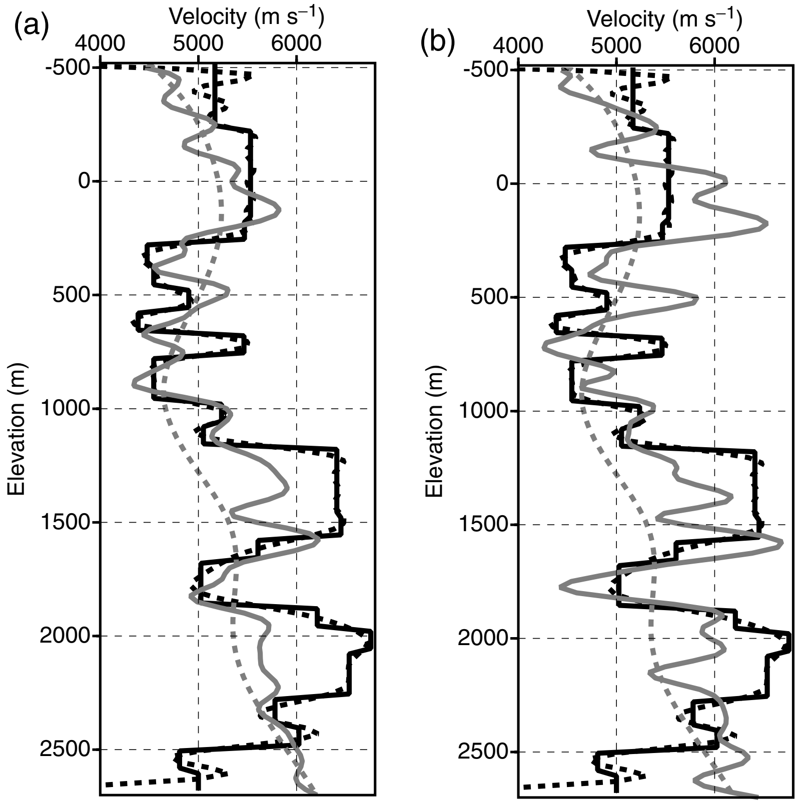

Figure 15. Comparison between VSP and traveltime and waveform tomography velocity logs: VSP log (solid black line), low-pass filtered VSP log (dotted black line), traveltime inversion log (dotted grey line), waveform inversion log (solid grey line). (a) The waveform inversion log was extracted from model of Fig. 14(a) (frequency component 20.06 Hz). (b) The waveform tomography log was extracted from the model of Fig. 14(b).

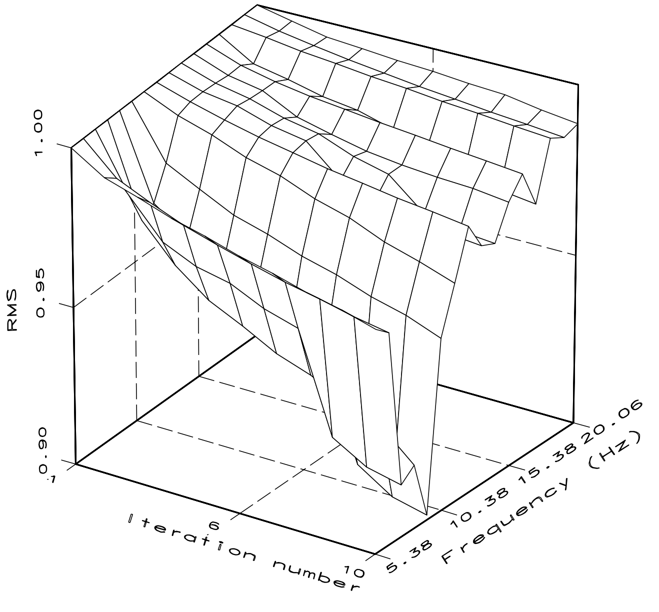

Figure 16. RMS as a function of iteration number and frequency. Each iteration number–RMS curve has been normalized by its maximum value.

frequency-domain data set is shown in the source–receiver position space at the dominant 10 Hz frequency component. We show the data at this intermediate frequency because the main geological features are already visible after the inversion of this frequency (Fig. 11b) and the phase spectra are easier to interpret at this frequency than at higher frequencies. This display allows us to view an example of a full monochromatic data set processed by the waveform tomography program. This frequency-domain representation doesn't allow a detailed analysis of arrivals since location in time is lost in the frequency domain. However, it helps us to diagnose whether or not the data fit is of equal quality all over the whole source–receiver domain.

The spectral amplitude of the observed data is shown in Fig. 18(a). For receiver positions located between 3 and 6 km distance (receivers around the one shown in Fig. 7) one can observe some amplitude highs for shots located at distances between 6 and 8 km, followed by an amplitude attenuation at distances between 9 and 11 km and a second amplitude high at distances between 11 and 13 km. This amplitude versus offset trend can be correlated with the shallow wide-angle reflection R1 which contributes to the first amplitude high, the shadow zone SZ and the wide-angle reflection R2 interpreted in Fig. 7. The spectral amplitude of synthetic data computed in the traveltime tomography model and the waveform tomography model of Fig. 11(b) are shown in Figs 18(d) and (b) respectively. The amplitude versus offset trend is better reproduced in the data computed in the waveform tomography model (Fig. 18b) than in the traveltime tomography one (Fig. 18d), although the amplitudes remained significantly underestimated in the two synthetic modulus maps (see the scales). Comparison between the observed phase (Fig. 18a) and phases computed in the traveltime (Figs 18d, e) and waveform tomography (Figs 18b, c) models shows that the phase misfit has been significantly lowered.

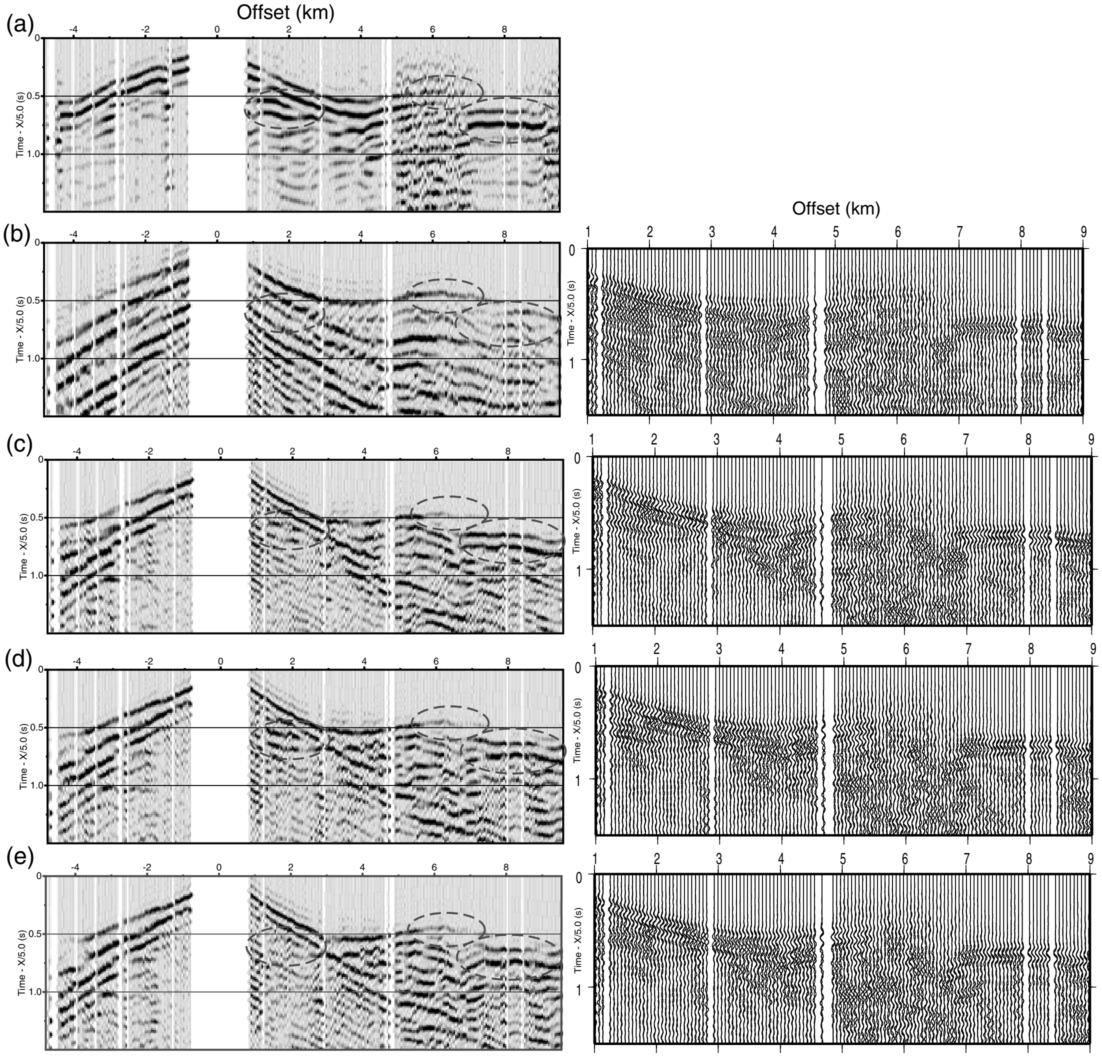

Figure 17. Comparison in the time domain between observed and computed seismograms. (a) Observed data after waveform tomography pre-processing corresponding to the CRG of Fig. 7. (b) Left: synthetic seismograms computed in the velocity model inferred from traveltime tomography. The match of the main features (wide-angle reflection R1, shadow zone, wide-angle reflection R2) delineated by the ellipses is discussed in the text. Right: direct comparison between observed (grey lines) and synthetic (black line) seismograms. (c) Left: synthetic seismograms computed in the velocity model of Fig. 11(b). Right: direct comparison between observed (grey lines) and synthetic (black line) seismograms. (d) Left: synthetic seismograms were computed in the velocity model of Fig. 11(c). Right: direct comparison between observed (grey lines) and synthetic (black line) seismograms. (e) Left: synthetic seismograms were computed in the velocity model of Fig. 11(d). Right: direct comparison between observed (grey lines) and synthetic (black line) seismograms.

GEOLOGICAL DISCUSSION OF THE FINAL MODEL

The small wavelength content of the velocity model resulting from the full-waveform tomography provides new insights into the structure of the upper crust and contributes to a better understanding of the internal geometry of the investigated thrust and fold system, which is instead only poorly imaged by conventional reflection seismic (Dell'Aversana 2001) (Fig. 6).

In the central part of the velocity model, the most noticeable features are southwest-dipping slices clearly delineated by high-velocity bodies (5500–6500 m s^{-1}) and narrow low-velocity regions (3500–4000 m s^{-1}) (Fig. 19a). Beneath the western flank of the antiform, these slices are cross-cut by a subvertical body, with velocities ranging from 4500 to 5500 m s^{-1}, which merges upwards with an evident near-surface high-velocity bump.

Both flanks of the antiform are characterized by near-surface low-velocity layers (2000–3000 m s^{-1}). The low-velocity layers reach a maximum thickness of about 1 km over distances between 5 and 7 km and overlie a region showing a quite chaotic succession of low- and intermediate-velocity layers which hamper the identification of large-scale velocity structures. Nevertheless, a low-velocity region (3500–4000 m s^{-1}) can be identified at a distance of about 4–5 km in the 1–2.5 km depth range.

The reliability of the full-waveform tomography velocity model has been further assessed by a comparison with a 2-D resistivity model obtained by Dell'Aversana (2001) inverting magnetotelluric data collected along the seismic profile (Fig. 19b).

We found a good agreement between the velocity and resistivity images. The southwest-dipping high-velocity bodies imaged at 1–2 km depth are consistent with two high-resistivity regions showing the same trend, while the high-velocity bump imaged beneath

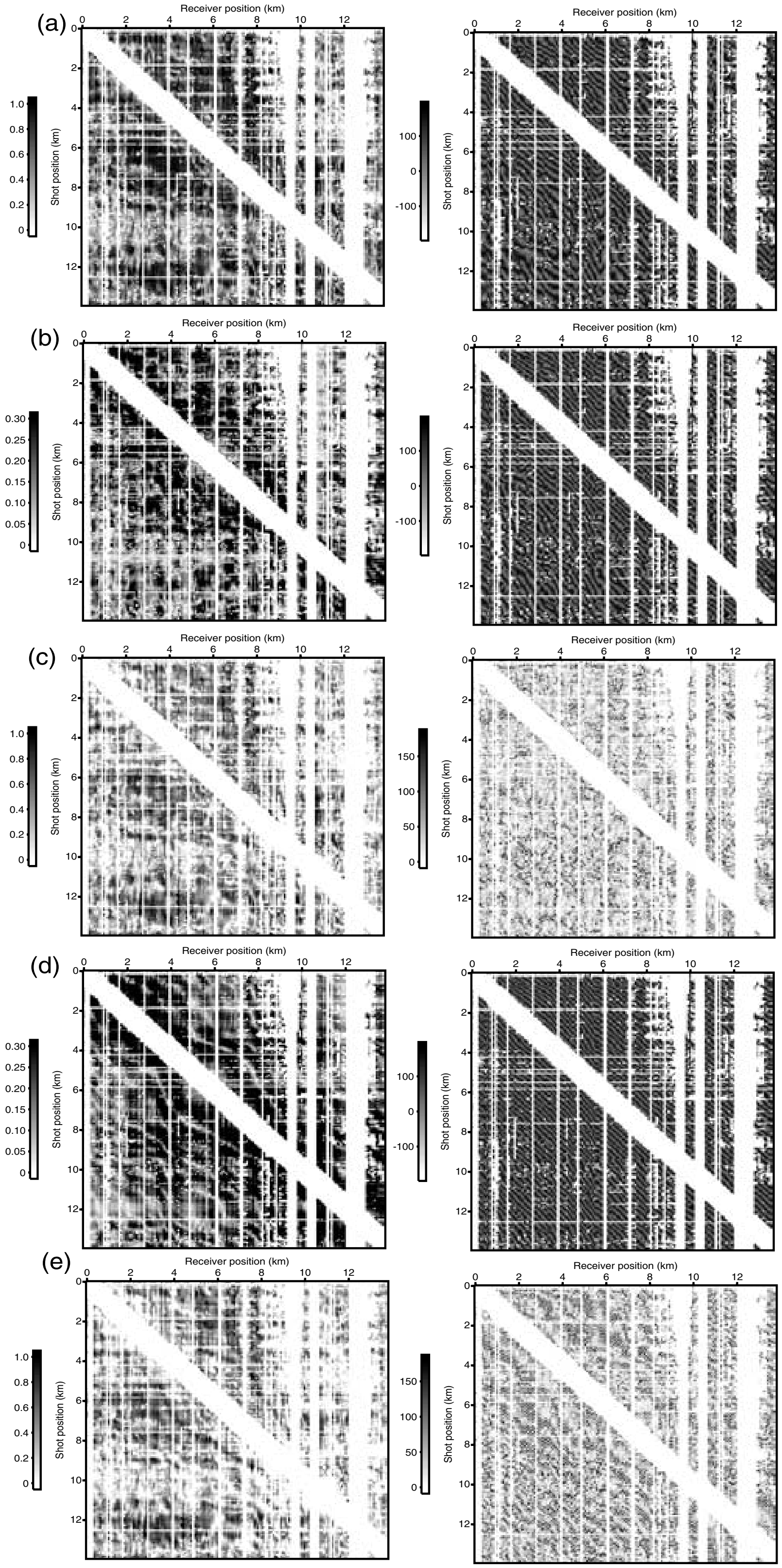

Figure 18. (a) Ten hertz observed data set displayed in the source–receiver domain. The spectral amplitude is plotted on the left and the phase is plotted on the right. (b) Ten hertz synthetic data computed in the waveform tomography model obtained close to the 10 Hz frequency component inversion. The same display as that of part (a) is used except that the scale spans a narrower range. (c) Difference between spectral amplitude and phase of parts (a) and (b). (d) Ten hertz synthetic data computed in the traveltime tomography model. The same display and scale are used as in part (b). (e) Difference between spectral amplitude and phase of parts (a) and (d).

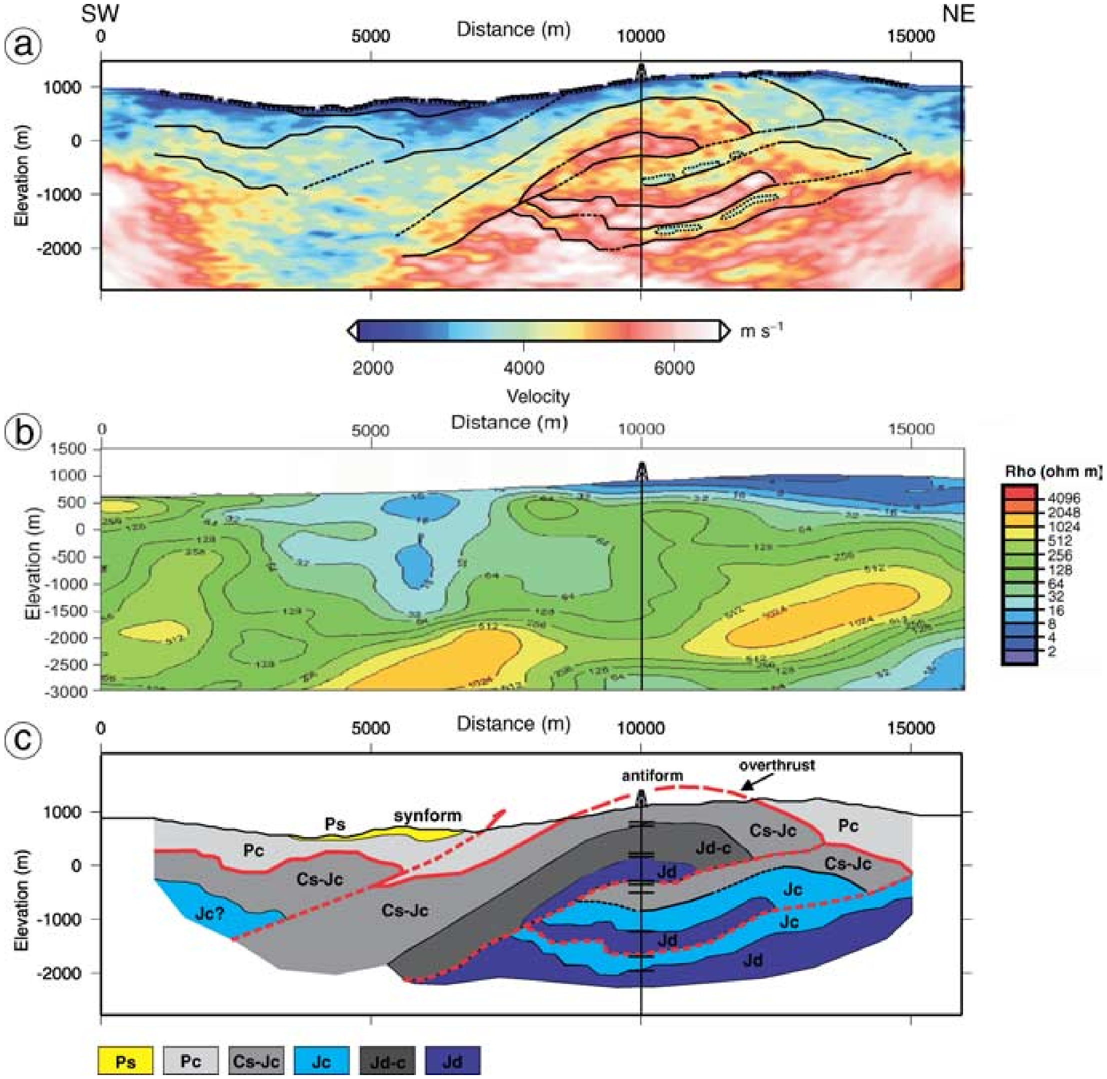

Figure 19. Geostructural interpretation of the waveform tomography model. (a) Main discontinuities (sharp velocity changes are indicated by black solid lines) and very low velocity contrasts (dotted black lines) used for the geological interpretation of the velocity model shown in Fig. 9(d). The discontinuities are locally constrained by well logs. (b) 2-D resistivity model obtained by inverting magnetotelluric data collected along the seismic profile (modified after Dell'Aversana 2001). Note the good agreement between the velocity and resistivity images. (c) Schematic geostructural interpretation of the velocity model: Ps, Pliocene soft sediments; Pc, Palaeocene clayey sediments; Cs-Jc, Cretaceous shales and Jurassic cherts; Jc, Jurassic cherts; Jd-c, strongly fractured Triassic cherty dolomites and cherts; Jd, stiff cherty dolomites. The main thrust planes (dashed lines) and the overthrust of the Palaeocene nappe (continuous line) are indicated. The geological discontinuities are constrained by the well data.

the antiform matches quite well a high-resistivity shallow region. The near-surface low-velocity layers bounding the antiform match well strongly conductive bodies. In particular, note the pronounced thickening of the conductive body imaged between 5 and 7 km distance. Finally, the low-velocity region identified in the deeper part of the model at about 4–5 km distance corresponds to a region of relatively low resistivity values sandwiched between two high-resistivity bodies.

A schematic geostructural interpretation of the velocity model is shown in Fig. 19(c). The geological interpretation, which is locally constrained by well data, is also based on the combined analysis of the velocity and resistivity images. In addition, surface geological mapping (Fig. 5) and some shallow reflectors imaged by conventional reflection seismograms (Fig. 6), facilitate the interpretation of the near-surface velocity structure.

We interpret the anticline explored by the well as a stack of two main southwest-dipping sheets, which are in turn cross-cut by an out-of-sequence thrust. The out-of-sequence thrust, which we relate to the main discontinuity drilled at about 0.3 km depth, is responsible for a tectonic doubling, as well as for the formation of a wide nappe anticline in the shallow part of the crust. The internal geometry of the anticline is well delineated by the high-velocity (5500–6500 m s^{-1}) and high-resistivity slices, which correspond to cherty dolomites (Fig. 19c). As inferred from the well data, the bottom of the high-velocity slices delineates the main thrust planes. Intermediate-velocity bodies are associated with cherts and/or strongly fractured dolomites, while the regions showing a chaotic succession of low- and intermediate-velocity layers may be indicative of sequences lithologically dominated by Cretaceous shales. This hypothesis is based on surface and well data, and is further supported by the presence of low-resistivity regions ($<100\ \Omega$ m), which suggest the presence of clayey materials.

Finally, we relate the near-surface low-velocity and strongly conductive layers to the regional nappe mainly composed of Cenozoic clays, which overthrusts the Mesozoic terrains. On the western side of the model, geological interpretation of the shallow structure is aided by conventional reflection data showing strong and quite continuous events at about 500 ms (Fig. 6). In particular, both the velocity and resistivity images contain hints of a thrust structure at about 5 km, which may be related to southwest-dipping events and truncated reflections in the stack section.

CONCLUSION

We have presented an application of frequency-domain full-waveform tomography to real onshore wide-aperture seismic data recorded in a complex geological environment (a thrust belt). Frequency-domain full-waveform tomography applied to dense wide-aperture data was tested as an alternative to near-vertical reflection data migration which gave poor result in the area. By inverting iteratively discrete frequency components from low to high values, the approach defines a multiscale imaging in the sense that high wavenumbers are progressively incorporated (non-linearly) in the velocity model. At the end, the velocity model contains a broad and continuous spectrum of wavelengths (i.e. a velocity model which incorporates both the large wavelength of the starting velocity model and the small wavelengths as the ones classically obtained by migration of reflection events).

The starting model required to initiate the full-waveform tomography was developed by non-linear first-arrival traveltime tomography. The results suggest that, at least locally, this starting model is sufficiently accurate to allow a good focalization of the wide-angle reflections.

The reliability of the velocity model derived from waveform tomography was first verified locally by comparison with a VSP log available on the profile. The 2-D velocity structure obtained by waveform tomography was also correlated with a 2-D resistivity section developed previously by Dell'Aversana (2001). Comparison between time-domain finite-difference seismograms computed in the velocity models obtained by traveltime and waveform tomographies allow us to demonstrate unambiguously that the waveform inversion successfully processes wide-angle reflections coming from the previously interpreted geological features.

Although the waveform tomography successfully imaged existing structures, the fit between observed and computed seismograms remains poor. Future work will primarily concern improvement of the waveform tomography pre-processing sequence which is crucial for obtaining reliable inversion results. Data weighting which can be equally applied to the observed and computed data can be improved such that each trace makes a significant contribution to the imaging. Different strategies for estimating the source function can be investigated. Moreover, some amplitude corrections (i.e. pressure to vertical particle velocity conversion, 3-D to 2-D conversion) still need to be improved or applied even if it is difficult to anticipate whether incorporation of these effects will significantly improve the imaging. Finally, the data weighting will also have to preserve the amplitude versus offset information such that more subtle amplitude effects can be tentatively accounted for in the framework of multiparameter waveform tomography incorporating as a first stage the attenuation in addition to *P*-wave velocity for model parametrization.

ACKNOWLEDGMENTS

This work benefited from fruitful discussions with J. X. Dessa. We would like to thank C. Zelt and an anonymous reviewer for their valuable comments. We thank Enterprise Oil Italiana for providing the data and the VSP log. Partial funding has been provided by the CEP& M G 5204/04. This paper is contribution number 682 of the UMR Géosciences Azur 6526.

REFERENCES

Aminzadeh, F., Burehard, N., Nicoletis, L., Rocca, F. & Wyatt, K., 1995. SEG/EAEG 3-D modeling project: third report, *The Leading Edge,* **14,** 125–128.

Berenger, J.-P., 1994. A perfectly matched layer for absorption of electromagnetic waves, *J. Comput. Phys.,* **114,** 185–200.

Chapman, C.H. & Orcutt, J.A., 1985. Least-square fitting of marine seismic refraction data, *Geophys. J. R. astr. Soc.,* **82,** 339–374.

Clayton, R. & Engquist, B., 1977. Absorbing boundary conditions for acoustic and elastic wave equations, *Bull. seism. Soc. Am.,* **67**(6), 1529–1540.

Crase, E., Pica, A., Noble, M., McDonald, J. & Tarantola, A., 1990. Robust elastic non-linear waveform inversion: application to real data, *Geophysics,* **55,** 527–538.

Crase, E., Wideman, C., Noble, M. & Tarantola, A., 1992. Nonlinear elastic inversion of land seismic reflection data, *J. geophys. Res.,* **97,** 4685–4705.

Davis, T.A. & Duff, I.S., 1997. *A Combined Unifrontal/Multifrontal Method for Unsymmetric Sparse Matrices,* Technical Report TR-97-016, University of Florida.

Dell'Aversana, P., 2001. Integration of seismic, MT and gravity data in a thrust belt interpretation, *First Break,* **19,** 335–341.

Dell'Aversana, P., Ceragioli, E., Morandi, S. & Zollo, A., 2000. A simultaneous acquisition test of high-density 'global offset' seismic in complex geological settings, *First Break,* **18**(3), 87–96.

Dessa, J.X. & Pascal, G., 2003. Combined traveltime and frequency-domain seismic waveform inversion: a case study on multi-offset ultrasonic data, *Geophys. J. Int.,* **154**(1), 117–133.

Gauthier, O., Virieux, J. & Tarantola, A., 1986. Two-dimensional nonlinear inversion of seismic waveforms: numerical results, *Geophysics,* **51**(7), 1387–1403.

Glangeaud, J.L.M.F. & Coppens, F., 1997. *Traitement du Signal pour Géologues et Géophysiciens,* Editions TECHNIP, Paris, France.

Gray, S.H., Etgen, J., Dellinger, J. & Whitmore, D., 2001. Seismic migration problems and solutions, *Geophysics,* **66**(5), 1622–1640.

Herrero, A., Zollo, A. & Virieux, J., 1999. Two-dimensional non linear first-arrival time inversion applied to Mt. Vesuvius active seismic data (TomoVes96), in *24th General Assembly, Abstract Book,* European Geophysical Society, The Hague.

Hicks, G.J. & Pratt, R.G., 2001. Reflection waveform inversion using local descent methods: estimating attenuation and velocity over a gas-sand deposit, *Geophysics,* **66**(2), 598–612.

Hobro, J.W.D., Singh, S.C. & Minshull, T.A., 2003. Three-dimensional tomographic inversion of combined reflection and refraction seismic traveltime data, *Geophys. J. Int.,* **152,** 79–93.

Hustedt, B., Operto, S. & Virieux, J., 2004. Mixed-grid and staggered-grid finite-difference methods for frequency-domain acoustic wave modelling, *Geophys. J. Int.,* **157,** 1269–1296.

Improta, L., Zollo, A., Herrero, A., Frattini, R., Virieux, J. & Dell'Aversana, P., 2002. Seismic imaging of complex structures by non-linear traveltime inversion of dense wide-angle data: application to a thrust belt, *Geophys. J. Int.,* **151,** 264–278.

Jannane, M. *et al.,* 1989. Wavelengths of Earth structures that can be resolved from seismic reflection data, *Geophysics,* **54**(7), 906–910.

Jo, C.-H., Shin, C. & Suh, J.H., 1996. An optimal 9-point, finite-difference, frequency-space, 2-D scalar wave extrapolator, *Geophysics,* **61**(2), 529–537.

Korenaga, J., Holbrook, W.S., Kent, G.M., Kelemen, P.B., Detrick, R.S., Larsen, H.C., Hopper, J.R. & Dahl-Jensen, T., 2000. Crustal structure of the southeast Greenland margin from joint refraction and reflection seismic tomography, *J. geophys. Res.,* **105,** 21 591–21 614.

Lambaré, G., Virieux, J., Madariaga, R. & Jin, S., 1992. Iterative asymptotic inversion of seismic profiles in the acoustic approximation, *Geophysics,* **57,** 1138–1154.

Lambaré, G., Operto, S., Podvin, P., Thierry, P. & Noble, M., 2003. 3-D ray + Born migration/inversion—part 1: theory, *Geophysics,* **68,** 1348–1356.

Lutter, W.J., Nowack, R.L. & Braile, L.W., 1990. Inversion of crustal structure using reflections from the PASSCAL Ouachita experiment, *J. geophys. Res.,* **95,** 4633–4646.

Operto, S., Xu, S. & Lambaré, G., 2000. Can we quantitatively image complex models with rays?, *Geophysics,* **65**(4), 1223–1238.

Operto, S., Lambaré, G., Podvin, P., Thierry, P. & Noble, M., 2003. 3-D ray + Born migration/inversion—part 2: application to the seg/eage overthrust experiment, *Geophysics,* **68,** 1357–1370.

Pica, A., Diet, J.P. & Tarantola, A., 1990. Nonlinear inversion of seismic reflection data in laterally invariant medium, *Geophysics,* **55**(3), 284–292.

Podvin, P. & Lecomte, I., 1991. Finite difference computation of traveltimes in very contrasted velocity model: a massively parallel approach and its associated tools, *Geophys. J. Int.,* **105,** 271–284.

Pratt, R.G., 1999. Seismic waveform inversion in the frequency domain, part 1: theory and verification in a physical scale model, *Geophysics,* **64,** 888–901.

Pratt, R.G. & Goulty, N.R., 1991. Combining wave-equation imaging with traveltime tomography to form high-resolution images from crosshole data, *Geophysics,* **56**(2), 204–224.

Pratt, R.G. & Shipp, R.M., 1999. Seismic waveform inversion in the frequency domain, Part 2: fault delineation in sediments using crosshole data, *Geophysics,* **64,** 902–914.

Pratt, R.G. & Worthington, M.H., 1990. Inverse theory applied to multi-source cross-hole tomography. Part 1: acoustic wave-equation method, *Geophys. Prospect.,* **38,** 287–310.

Pratt, R.G., Song, Z. & Warner, M., 1996. Two-dimensional velocity models from wide-angle seismic data by wavefield inversion, *Geophys. J. Int.,* **124,** 323–340.

Pratt, R.G., Shin, C. & Hicks, G.J., 1998. Gauss–Newton and full Newton methods in frequency-space seismic waveform inversion, *Geophys. J. Int.,* **133,** 341–362.

Sheriff, R.E. & Geldart, L.P., 1995. *Exploration Seismology,* Cambridge University Press, Cambridge.

Shin, C., Yoon, K., Marfurt, K.J., Park, K., Yang, D., Lim, H.Y., Chung, S. & Shin, S., 2001. Efficient calculation of a partial derivative wavefield using reciprocity for seismic imaging and inversion, *Geophysics,* **66**(6), 1856–1863.

Shipp, R.M. & Singh, S.C., 2002. Two-dimensional full wavefield inversion of wide-aperture marine seismic streamer data, *Geophys. J. Int.,* **151,** 325–344.

Sirgue, L. & Pratt, R.G., 2001. Frequency-domain waveform inversion: a strategy for choosing frequencies, in *63rd Annual Meeting, EAGE, Expanded Abstracts, Abstract No. p014,* pp. 631–634, Eur. Assoc. Explor. Geophys., Houten, the Netherlands.

Stekl, I. & Pratt, R.G., 1998. Accurate viscoelastic modeling by frequency-domain finite differences using rotated operators, *Geophysics,* **63**(5), 1779–1794.

Sun, R. & McMechan, G.A., 1992. 2-D full-wavefield inversion for wide-aperture, elastic, seismic data, *Geophys. J. Int.,* **111,** 1–10.

Tarantola, A., 1984. Inversion of seismic reflexion data in the acoustic approximation, *Geophysics,* **49**(8), 1259–1266.

Tarantola, A., 1987. *Inverse Problem Theory: Methods for Data Fitting and Model Parameter Estimation,* Elsevier, Amsterdam.

Thierry, P., Operto, S. & Lambaré, G., 1999. Fast 2D ray–Born inversion/migration in complex media, *Geophysics,* **64**(1), 162–181.

Toksoz, M. & Johnston, D., 1981. *Seismic Wave Attenuation,* Society of Exploration Geophysicists, Tulsa, OK.

Toomey, D.R., Solomon, S.C. & Purdy, G.M., 1994. Tomographic imaging of the shallow crustal structure of the east pacific rise at 9°30′N, *J. geophys. Res.,* **99,** 24 135–24 157.

Virieux, J., 1986. P-SV wave propagation in heterogeneous media, velocity-stress finite difference method, *Geophysics,* **51,** 889–901.

Williamson, P. & Pratt, G., 1995. A critical review of 2.5D acoustic wave modeling procedures, *Geophysics,* **60,** 591–595.

Zelt, C. & Barton, P.J., 1998. Three-dimensional seismic refraction tomography: a comparison of two methods applied to data from the Faeroe basin, *J. geophys. Res.,* **103**(B4), 7187–7210.

Zelt, C. & Smith, R.B., 1992. Seismic traveltime inversion for 2-D crustal velocity structure, *Geophys. J. Int.,* **108,** 16–34.